VISCOUS FLOW AND CRYSTALLIZATION OF BULK METALLIC GLASS FORMING LIQUIDS

Thesis by

Andreas Masuhr

In Partial Fulfillment of the Requirements

for the Degree of

Doctor of Philosophy

California Institute of Technology

Pasadena, California

1999

(submitted December 8, 1998)

To Susanne

ACKNOWLEDGMENTS

I am grateful to Professor Bill Johnson for giving me the opportunity to pursue my Ph.D. at Caltech. It has been a privilege to work with him and experience his unparalleled intuition for science. I thank him for giving me the freedom to explore the subject and for his faith in my abilities and decisions.

A special thanks goes to Ralf Busch for his continuing support and for making the last four years enjoyable. Parts of the experimental work were made possible through fruitful collaborations with Eric Bakke, Achim Rehmet, Andy Waniuk, Jan Schroers, and the invaluable help of Mike Gerfen. My memories are with Y.J. Kim who helped to get my research project started in 1994.

I profited from many stimulating discussions with Ulrich Geyer, Susanne Schneider, Atakan Peker, Mo Li, Konrad Samwer, Helmut Mehrer, Kathrin Knorr, and many others. Also, I would like to thank all members of the Materials Science Group for making my stay at Caltech a wonderful experience.

The financial support from the Department of Energy under grant No. DE-FG-03-86ER45242 and from the ALCOA Technical Center is greatly appreciated.

Finally, I would like to acknowledge the support and encouragement of my parents and my wife Susanne. None of this work would have been possible without them.

ABSTRACT

An experimental setup was designed and implemented to measure the flow behavior of liquids in the viscosity range from 10^{-1} Pa s to 10^{4} Pa s. The viscosity of the $Zr_{41.2}Ti_{13.8}Cu_{10.0}Ni_{12.5}Be_{22.5}$ (V1) bulk metallic glass forming alloy was measured over a temperature range from 927 K to 1173 K. At the liquidus temperature, the viscosity is 2.3 Pa s, which is about three orders of magnitude larger than the viscosity of a pure metallic liquid. The free volume theory as formulated by Cohen and Grest describes the temperature dependence of the viscosity of V1 over 14 orders in magnitude.

The high viscosity of V1 above the liquidus temperature stabilizes the liquid against convective flow due to temperature gradients and allows for diffusion experiments in the equilibrium liquid. The temperature dependence of the diffusivity of large atoms like Al or Au scales with the viscosity. The time scales obtained from the viscosity measurements suggest that above the calorimetric glass transition region the diffusion of small and medium sized atoms is governed by thermally activated jumps.

Liquid V1 could be successfully supercooled inside high purity graphite crucibles without changing the stability of the supercooled liquid with respect to crystallization compared to levitated samples. The sluggish kinetics that are reflected in the high viscosity in the supercooled liquid state contribute significantly to the good glass forming ability of the alloy. The critical cooling rate is about 1 K/s.

The onset of crystallization under isothermal conditions as well as upon heating from the amorphous state was studied in detail. The critical heating rate to bypass crystallization was measured to be 200 K/s and the difference between the critical cooling and critical heating rate can be qualitatively understood in the framework of nucleation and growth.

However, the observed deviations from classical steady state nucleation behavior indicate a more complex crystallization mechanism. Rheological and crystallization studies at constant shear rate suggest that changes in the morphology of the supercooled liquid of V1 occur as a precursor of crystallization.

CONTENTS

FIGURES

1. INTRODUCTION

In thermodynamic equilibrium, a one component substance may be present as a crystal or a fluid. As shown in the pressure-temperature, p-T, phase diagram in Fig 1 (a), a distinction between the liquid and gaseous state is strictly justifiable only along the vapor pressure curve, where the two states of matter can be found in co-existence. At ambient pressure, indicated by the dotted line in Fig 1 (a), however, a distinction between the three states, crystalline, liquid, and gaseous, is appropriate and will be used in the following.

Quantum mechanics and statistical mechanics give a mathematical framework to relate the macroscopic properties of a substance to its microscopic structure and dynamics. The periodicity of a perfect crystal at $T = 0$ on the one hand, and the stochastic behavior of atoms in an ideal gas for $T \to \infty$ on the other, yield simple analytical expressions for the equations of state for these two states of matter. For the liquid state, the notion of an 'ideal liquid' based on a simple and mathematically tractable model has not yet been established [1]. Models based on hard spheres or other pair potentials may serve as a substitute, particularly in computer simulations, but have not reached the degree of universality as the theories of crystals and gases.

Experimentally, the transformation from the liquid to the crystalline state may be suppressed for extended periods of time when the liquid is cooled below its melting point ('supercooling') [2]. The physical properties of the liquid are continuous across the melting point, and the system can be found in metastable equilibrium for extended temperature ranges. Fig 1 (b) schematically shows the specific volume

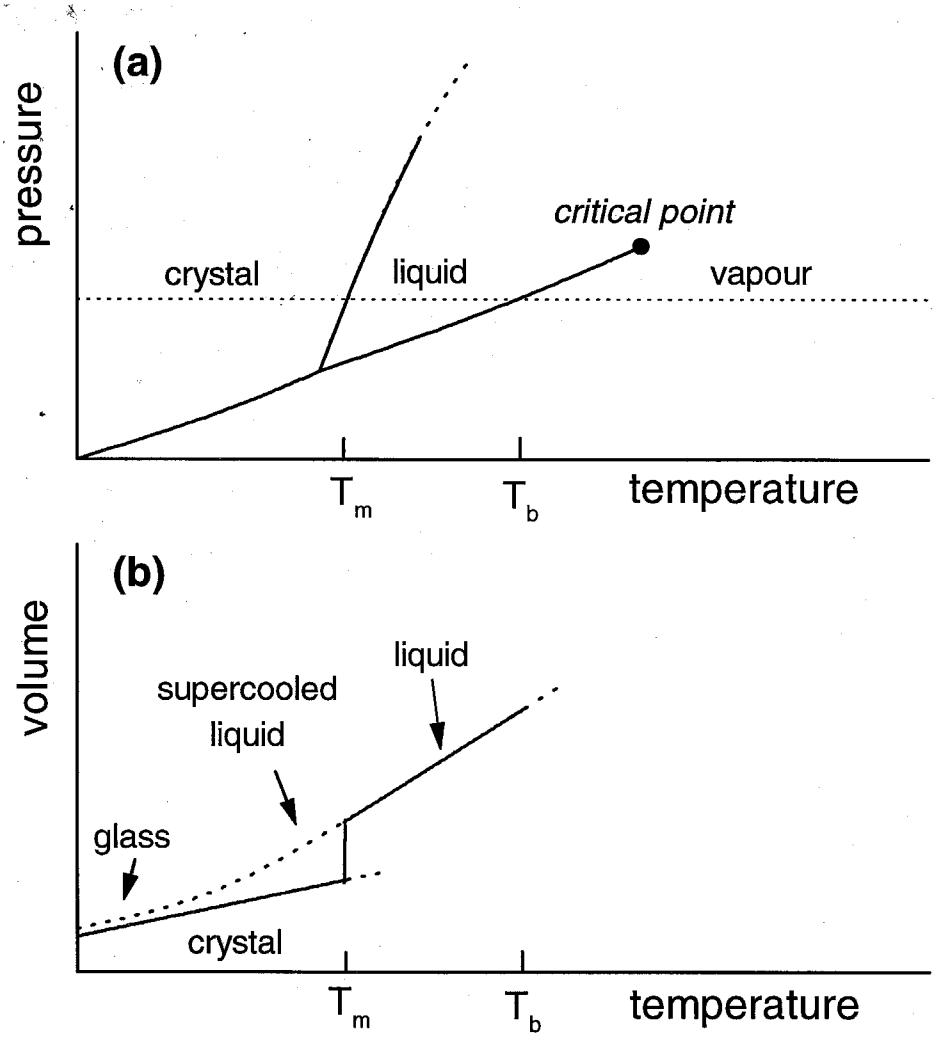

Fig. 1 The crystalline, gaseous, and liquid state

(a) Crystalline and fluid phase regions as a function of pressure and temperature. The crystalline, liquid, and gaseous phases at ambient pressure (···) are indicated. (b) Temperature dependent specific volume of the crystalline and liquid phase (—) as well as of the supercooled liquid and the glass (···). The melting temperature, T_m, and the boiling temperature, T_b, at ambient pressure are marked.

versus temperature curve for a one-component substance. Below the glass transition region, the volume shows a weaker temperature dependence than expected from an extrapolation of the high temperature values. It is important to note that the temperature range in which the glass transition can be observed experimentally depends on the cooling rate that is applied to the liquid.

With the liquid state an average internal relaxation time is associated that describes the time scale on which the system samples its available phase space in (metastable) thermodynamic equilibrium. While for equilibrium liquids this time is often found to be less than 10^{-9} s, it increases dramatically in the supercooled liquid. A continuous increase of more than 14 orders of magnitude in the relaxation time with decreasing temperature can be observed using, e.g., dielectric measurements. The viscosity increases – to a good approximation – proportional to this relaxation time, making it a macroscopic probe for rearrangements on a microscopic scale [3].

It is widely accepted that any liquid can - in principal - be quenched to the amorphous state by applying an appropriate 'critical' cooling rate to prevent significant crystallization. This rate may be as small as 10^{-3} K/s for good glass formers like commercial soda-lime-silica glasses. In order to form a metallic glass from a monatomic metallic liquid, the (estimated) critical cooling rate is as large as 10^{12} K/s [4]. Duwez [5] found that Au-Si alloys with near-eutectic composition can be quenched into the amorphous state with cooling rates of ca. 10^{6} K/s. These high rates allow only for the formation of foils with a maximum thickness of some 10 µm. Recently, multicomponent metallic alloys were found to form metallic glass with rates as small as 10^{-1} K/s resulting in bulk amorphous glass (BMG) with smallest

dimensions on the order of 1 cm. One of the important concepts in understanding the glass forming ability includes Turnbull's [4] discussion of the reduced glass transition temperature, T_g/T_m, and its influence on the nucleation kinetics.

In chapter 2, the experimental apparatus and procedure used to study the flow behavior and crystallization of Zr-based metallic alloys are described. Calibration procedures are presented and the importance of a compatible crucible material for the rheometric measurements is discussed in sub-chapters. In chapter 3.1 results from the high temperature viscometer on liquid $Zr_{41.2}Ti_{13.8}Cu_{10.0}Ni_{12.5}Be_{22.5}$ (V1) are presented. A model of the high temperature limit of the viscosity, discussed in chapter 3.2, yields a 'fix-point' in the discussion of the rheological properties of a wide range of liquids. It allows for a phenomenological classification of the present results in the framework of 'strong' and 'fragile' liquids. In the subsequent chapters, 3.3 and 3.4, the temperature dependence of the viscosity is analyzed according to entropy and free volume models for viscous flow. Results from Cohen and Grest's theory of the liquid state are used in chapter 4 to compare the time scales of viscous flow with relaxation times from calorimetric experiments and atomic transport data in the liquid and supercooled liquid.

Results from crystallization studies of V1 are presented in chapter 5. First, isothermal measurements of the onset of crystallization are analyzed in chapter 5.1 according to classical nucleation and growth theory. The difference in crystallization behavior upon cooling from the equilibrium melt on the one side and upon heating amorphous samples on the other, is the subject of chapter 5.2. A modification of the experimental apparatus, allowing for high heating rates and precise temperature

measurements, allows for an unprecedented temperature range of the supercooled liquid in a metallic system upon heating. Finally, results from crystallization studies at constant shear rate are presented and discussed in chapter 5.3.

2. EXPERIMENTAL

In most viscometers either the rotating (or oscillating) cylinder method or the capillary method is employed [6]. The resolution of capillary viscometers is, in general, superior to that of the rotating cylinder viscometers. While the first are primarily used for measuring low viscosity liquids with viscosities, η, of less than 1 Pa s, the latter are used for liquids with more sluggish flow behavior. There are no commercially available viscometers for liquid metals with melting points on the order of 1000 K. For the present work, an experimental setup was designed to simultaneously measure the flow behavior as well as heat releases upon crystallization and melting of metallic alloys with melting temperatures up to 1400 K.

Liquid metals are known to be susceptible to impurities like oxygen if processed in air or in an incompatible crucible. The effects of contaminations induced through the liquid surface or the container interface will decrease with increasing sample sizes and – in industrial applications - the purity of the bulk liquid may only be remotely dependent on the processing environment. On a laboratory scale with sample sizes of a few cm^3, however, the liquid has to be processed either in vacuum or under an inert atmosphere. The choice of a compatible crucible is equally important.

In the present work, the apparatus designed to process the liquid samples encloses a volume of approximately 3×10^{-6} m^3 or about 0.1 mole of an inert atmosphere at ambient pressure. For comparison, the mass of the graphite containers (shear cell) of ca. 60 g corresponds to 5 mole of carbon atoms and a typical sample of 30 g of V1 contains a total of 0.5 mole of atoms. The size of the container in conjunction with the

high atomic mobility of impurities in both the graphite and the sample at temperatures of more than 1000 K imply that the purity of the graphite is decisive for the purity of the metallic liquid. An impurity concentration of, e.g., 10^{-6} (1 ppm) in the solid or liquid state corresponds to a partial pressure of impurities in the atmosphere of 10^{-1} Pa.

2.1. Experimental Setup

Viscosity measurements are based on either pressure-driven (Poiseuille) flow or wall-driven (Couette) flow of the fluid under inspection [7, 8]. Experiments employing steady state Poiseuille flow through quartz capillaries will be briefly discussed in chapter 2.4 while in the following the setup for viscosity measurements involving wall-driven flow between concentric cylinders is desribed.

At the heart of the high temperature Couette viscometer that is shown in Fig 2 and Fig 3 is the shear cell, consisting of a cylindrical crucible (outer cylinder) and a concentric rotating bob (inner cylinder). The liquid metal fills the space between the two cylinders. Under continuous rotation of the inner cylinder, a steady-state flow field is established within the liquid, resulting in a static torque on the fixed outer cylinder. For a Newtonian fluid, this torque is proportional to the shear viscosity coefficient of the liquid as will be shown in chapter 2.2.

As all graphite parts used in this work, both cylinders are machined from graphite, grade *DFP-1*, supplied by *POCO Graphite, Inc.* The graphite is attached to titanium (99.9%) adapters. Besides giving ample mechanical support up to temperatures of 1400 K, the titanium parts serve as a getter for residual oxygen. A stainless steel shaft connects the titanium adapter of the inner cylinder to a ferrofluid feedthrough, type

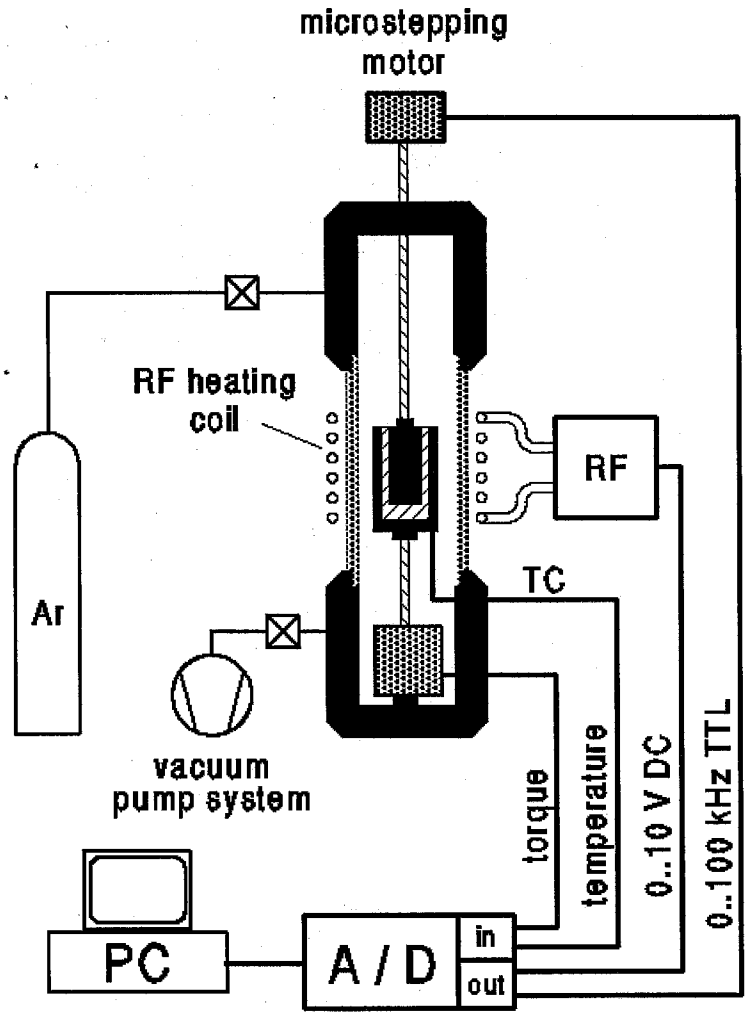

Fig. 2 Experimental setup of the high temperature viscometer

Two concentric cylinders are mounted inside the vacuum chamber and are inductively heated by the RF heating coil. A static torque sensor is positioned at the bottom of the chamber. A microstepping motor is mounted on a vertical drive (not shown) and is connected to the rotating, inner graphite cylinder through a ferrofluid feedthrough.

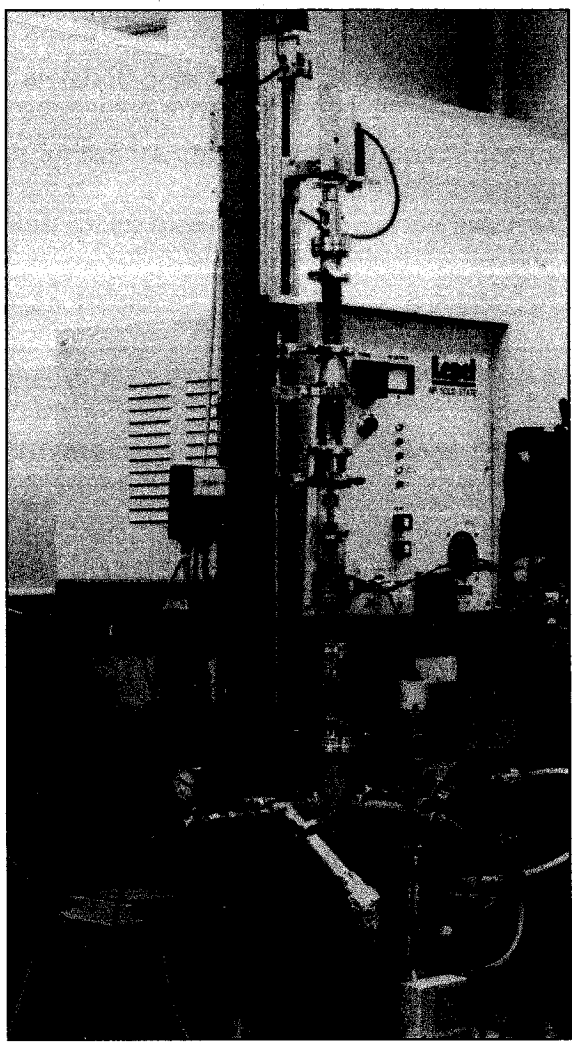

Fig. 3 Photograph of the high temperature viscometer

Experimental setup used for the high temperature rheometry and for the crystallization studies of V1 and V4. The photograph shows the shear cell's outer cylinder heated by the RF coil with the inner cylinder inserted into the liquid. An o-ring sustained ball bearing mount is attached to the rotating shaft above the shear cell to ensure concentric alignment of the two cylinders.

080-50C103912. A microstepping motor, type *P315-M233*, is attached to the air side of the feedthrough via an 82:50 gear and is driven by a *P315* microstep drive, supplied by *American Precision Industries, Inc.* The resolution of the drive of 50800 steps per revolution allows smooth rotary motion of the inner cylinder with angular frequencies from ca. 5×10^{-3} s^{-1} to 2×10^{2} s^{-1}.

The titanium adapter of the outer cylinder is connected to a static torque sensor at the bottom of the apparatus. Depending on the scope of the experiment, either an *Eaton 2121-100* or an *Eaton 2127-10* torque sensor is used for maximum torque readings of 100 Lbs-In. (1.15 Nm) and 10 Oz-In. (7.2×10^{-3} Nm). The torque sensor is mounted inside the vacuum chamber to avoid the influence of a feedthrough on the torque reading. Both sensors use four strain gauges each, mounted at 45° to the torque axis and wired in the form of a Wheatstone bridge. An *OMEGA DP41* signal conditioner that also processes the torque sensor signal supplies the excitation voltage of 24 V.

The graphite shear cell is inductively heated using a *Lepel MR-7.5* radio frequency (RF) power supply and a seven turn heating coil made out of 6.35 mm diameter copper tubing. The RF power supply has a maximum output of 7.5 kW at ca. 200 kHz. The RF coil is wound around the quartz tube enclosing the shear cell. In this way, RF vacuum feedthroughs are avoided and the coil's position can easiliy be adjusted to yield a homogeneous temperature distribution in the shear cell. The measured temperature as a function of the RF power supply setting is shown in Fig 4 for two different graphite crucibles. A type K thermocouple, *OMEGA SCAIN-040U-12-SHX*, is inserted into the outer cylinder's crucible wall, measuring the temperature

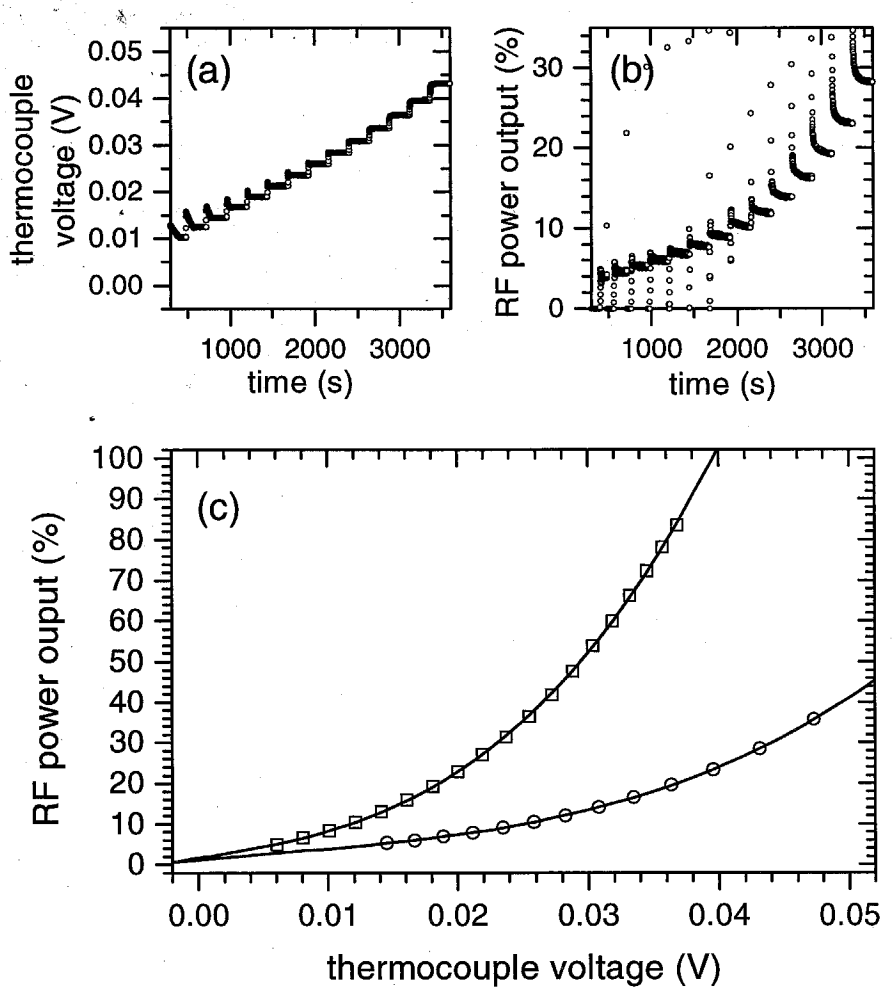

Fig. 4 Calibration of the RF power supply

(a) Thermocouple voltage measured as a function of time for a 31.8 mm diameter graphite crucible heated by a 62 mm diameter, 7-turn RF coil. The temperature is raised in steps of 50 K from 600 K to 1200 K. (b) Corresponding power setting of the RF power supply. (c) Power setting as a function of thermocouple voltage (○). For comparison, power settings for a 4 mm diameter graphite crucible heated by a 31 mm diameter, 5 turn RF coil are also shown (□). Solid lines in (c) are least-squares fits of third order polynomials to the data points.

of the shear cell [9]. Particular care has been given to a 'loose' placement of the lead wires of the thermocouple inside the vacuum chamber in order to minimize the resulting offset in the torque reading below the detection limit of the torque sensors of 3×10^{-6} Nm. Temperature gradients of ±4 K of the nominal temperature have been observed on the surface of the shear cell using a Leeds & Northrup 8622 pyrometer. The temperature reading of the thermocouple has been found to be in accordance with the melting points of Sn, Al, and Ag within ±0.5 K, ±0.5 K, and ±0.8 K, respectively.

The vacuum chamber was constructed using high vacuum components, supplied by *MDC Vacuum Products*. Flexible bellows support the metal-glass connectors attached to the ends of the quartz tube that surrounds the shear cell. A *Balzers TPG 064* turbo pump with a *TCP 015* drive unit, connected to the vacuum system, yields a vacuum of 8×10^{-2} Pa. The turbo pump is backed up by a *Leybold-Heraeus Trivac D2A* rotary pump equipped with a forline trap to prevent oil-backstreaming. High purity Ar (99.9999%) is used as an inert atmosphere in experiments, which require fast cooling rates. The Ar passes a heated titanium-sponge getter, supplied by *API Controls Division, Inc.*, before reaching the vacuum chamber. He (99.9999%) flow through an overpressure outlet valve (2.2×10^{5} Pa) may further increase the cooling rate of the graphite crucible up to 80 K/s.

The data acquisition system, schematically shown in Fig 5, is built around a *National Instruments AT-MIO-16E-50* multipurpose data acquisition board, installed in a PC, running *Labview 4.0*. Via a *National Instruments SCB-68* connector box, that contains a cold junction temperature sensor for the thermocouple readout, two

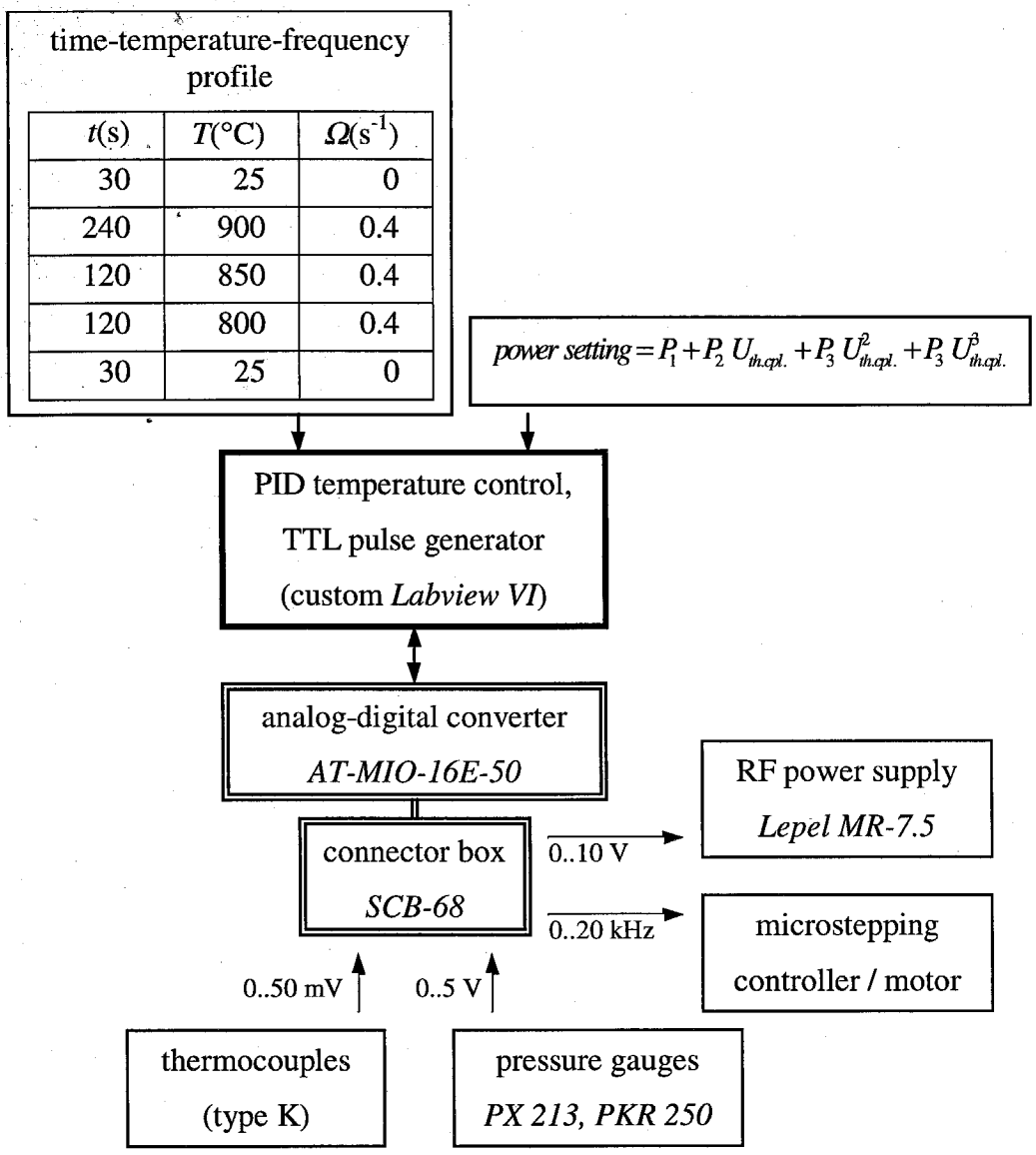

Fig. 5 Temperature control and data acquisition system

The custom written PID Labview VI compares the measured thermocouple voltages with the set points of the time-temperature-frequency profile. According to Eq. (1), a voltage (0..10 V) is applied to the remote input of the RF power supply. The 'power fit' eliminates the need to adjust the integrational parameter, I, in Eq. (1).

thermocouples, two pressure sensors, and the torque sensor are connected for data acquisition at 16 bit with a maximum sample rate of 20 kHz.

The first pressure gauge is an *OMEGA PX213* with an *OMEGA DP41* signal conditioner for total pressures of up to 3×10^5 Pa and for rough vacuum. For accurate high vacuum readings, the second gauge, a *Balzers PKR 250 Full Range Gauge* with readout unit *Balzers TPG 251*, is used.

The nominal temperature-time profile along with the desired rotation frequencies of the inner cylinder are programmed prior to the start of the experiment. The times, temperatures, and frequencies are contained in a spreadsheet that can easily be modified using, e.g., *ORIGIN 4.0.* The spreadsheet is read by a *Labview virtual instrument (VI)* that employs a modified proportional-integrational-differential (PID) control algorithm. Depending on the actual temperature measurement (thermocouple voltage, U_{th}) and the set-point temperature, U_{sp}, the PID algorithm computes a voltage (power setting) in the range from 0 V to 10 V, according to Eq. (1), that is applied to the remote control input of the *Lepel* RF power supply.

$$power\ setting = P\left(U_{th} - U_{sp}\right) + I\int_0^t \left(U_{th} - U_{sp}\right)dt + D\frac{d\left(U_{th} - U_{sp}\right)}{dt} \qquad (1)$$

To reduce the number of control parameters in the PID algorithm from three (P, I, D) to two (P, D), a so-called 'power-fit' is performed after the crucible or shear cell has been mounted. For this power-fit, the temperature is raised in steps of 50 K and the RF power output required to maintain the temperature is recorded. Examples are shown in Fig 4 (a) and Fig 4 (b). Typical results for the equilibrium power setting as a function of the thermocouple voltage, i.e., the temperature, are plotted in Fig 4 (c) for

two different crucibles. The smaller the difference between the radius of the heating coil and the outside diameter of the crucible, the more effectively is the RF power absorbed by the graphite. Third order polynomials are used to fit the power settings as a function of the thermocouple voltage in Fig 4 (c). The four fit Parameters (P_0, P_1, P_2, P_3) of the polynomial are fed into the PID algorithm, eliminating the need to adjust the integrational constant, I, in the PID loop in Eq. (1) by setting $I = 0$.

2.2. Concentric Cylinder Rheometry

The viscosity of glycerol, $C_3H_5(OH)_3$, has been measured previously and its temperature dependence around room temperature is well-established [2]. At 23°C the viscosity is $\eta = 2.8$ Pa s. As glycerol wets graphite, it may serve as a test fluid for the present concentric cylinder Couette viscometer. The following analysis of the flow field inside the shear cell is the basis for the viscosity measurements of V1.

The liquid fills the gap between the inner and the outer cylinders of the shear cell, with radii, R_1 and R_2, respectively. The inner cylinder rotates with angular frequency, Ω, while the outer cylinder is fixed. Assuming the no-slip boundary conditions

$$u_\theta(R_1) = \Omega R_1 \tag{2}$$

$$u_\theta(R_2) = 0 \tag{3}$$

the velocity in θ-direction, u_θ, within the liquid can be integrated from the equations of motion in radial and tangential direction [10]:

$$u_\theta = \frac{\Omega R_1^2}{R_2^2 - R_1^2}\left(\frac{R_2^2}{r} - r\right). \tag{4}$$

Using cylindrical coordinates (r, θ, z), the velocity in z- and r-direction is zero for the case of infinitely long cylinders:

$$u_z = u_r = 0. \tag{5}$$

At the flow velocities used in the present work, one can neglect the compressibility of the liquid. From Eq. (4) the radius dependent shear rate, $\dot{\gamma}$, can be calculated as

$$\dot{\gamma} \equiv \dot{\gamma}_{r\theta} = r\frac{\partial}{\partial r}\left(\frac{u_\theta}{r}\right) = -\frac{2R_1^2 R_2^2}{R_2^2 - R_1^2}\frac{1}{r^2}\Omega. \tag{6}$$

For small spacings between the two cylinders, i.e., for $(R_2\text{-}R_1) \ll R_1$, the variation of the shear rate with the radius, r, is small, and an average shear rate,

$$\dot{\gamma}_{ave} \equiv \dot{\gamma}\left(\frac{R_1 + R_2}{2}\right), \tag{7}$$

may be used. For, e.g., a shear cell with $R_1 = 11.11\times10^{-3}$ m, $R_2 = 12.70\times10^{-3}$ m used in the viscosity measurements of V1, the average shear rate in Eq. (7) is $\dot{\gamma}_{ave} \cong 0.177\,\Omega$.

For a Newtonian fluid, the shear stress, s, is proportional to the shear strain rate where the proportionality constant is called the shear viscosity coefficient, η:

$$s = \dot{\gamma}\,\eta. \tag{8}$$

At the wall ($r = R_2$) of the outer cylinder the shear stress (shear force per area) is

$$s(R_2) = \eta\dot{\gamma}(R_2) = -\frac{2R_1^2}{R_2^2 - R_1^2}\Omega\eta \tag{9}$$

and the static torque, M, on the outer cylinder is calculated from the shear stress at $r = R_2$ times the area, $2\pi R_2 L$, and the radius, R_2, of the outer cylinder:

$$M = \frac{4\pi L R_1^2 R_2^2}{R_2^2 - R_1^2}\Omega\eta. \tag{10}$$

Equation (10) relates the measured torque, M, to the viscosity, η, through the angular frequency, Ω, and the dimensions of the shear cell. It was derived by Couette [11], who also performed the first viscosity measurements using the concentric cylinder geometry. The ratio of the length, L, of the shear cell to the spacing between the cylinders, $L/(R_2\text{-}R_1)$, is typically on the order of 30 for the present shear cells.

For calibration, the torque meter is mounted horizontally outside the vacuum chamber and a horizontal bar of 12 cm length, attached to the torque meter, is loaded with standard weights. The corresponding torque sensor signals are plotted in Fig 6 as a function of the applied torque, M. A linear relation

$$M = 0.01446\ \frac{torque\ sensor\ signal}{\mathrm{V}}\ \mathrm{Nm} \tag{11}$$

is found to describe the data accurately over four orders of magnitude in torque.

The torque transferred through the glycerol to the outer cylinder ($R_2 = 12.70\times10^{-3}$ m) is plotted in Fig 7 as a function of the angular frequency of the inner cylinder. Two different inner cylinders were used with radii 6.35 mm and 12.7 mm, respectively. The resolution of the torque sensor allows for measurements down to 10^{-6} Nm. Plotted in the same figure is the torque calculated from Eq. (10)

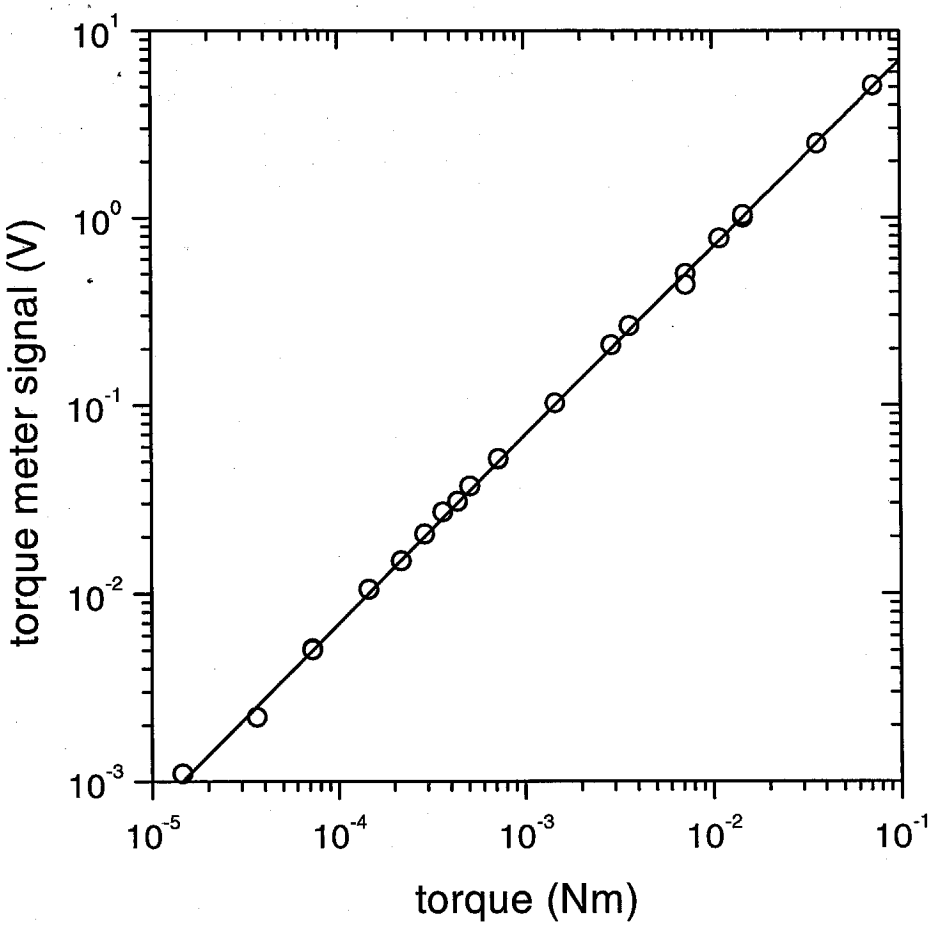

Fig. 6 Torque meter calibration curve

Static torques are applied by loading a 12 cm beam with standard weights. The amplified torque signal (○) using an OMEGA DP41 signal conditioner is well described by the linear relation, Eq. (11).

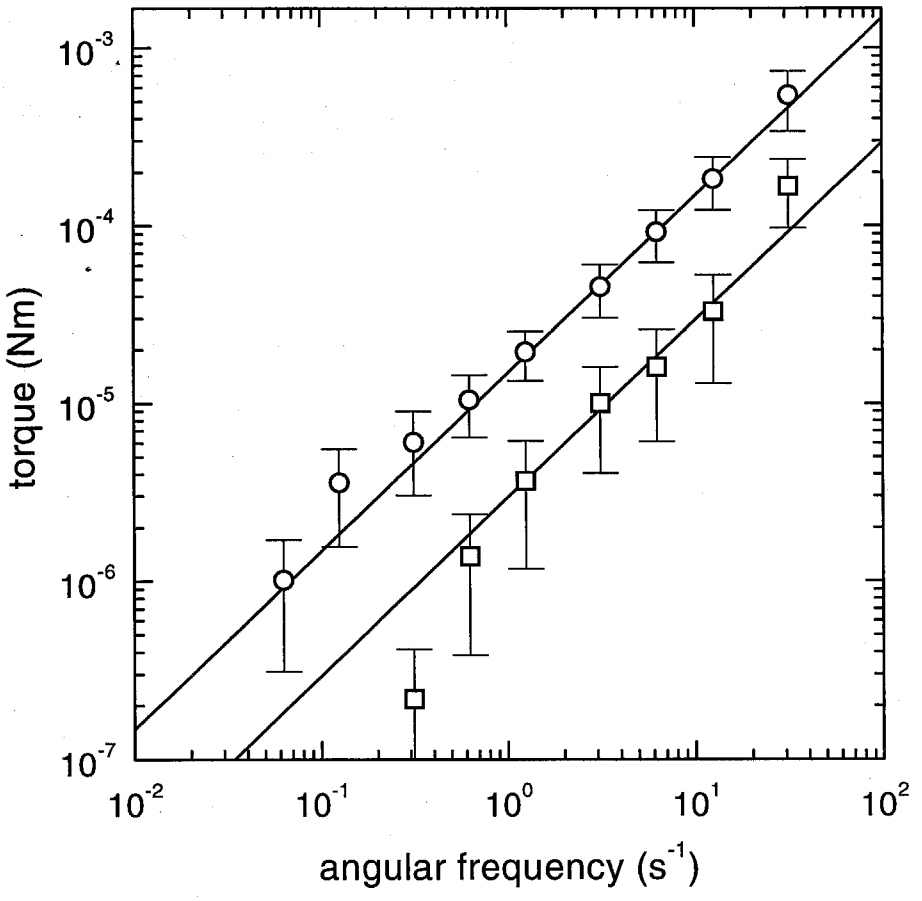

Fig. 7 Viscosity measurements of glycerol

Static torque reading on the outer cylinder ($R_2 = 12.70 \times 10^{-3}$ m) as a function of the rotation frequency of the inner cylinder at room temperature. Two different inner cylinders with radius $R_{1,a} = 11.11 \times 10^{-3}$ m (○) and $R_{1,b} = 6.35 \times 10^{-3}$ m (□) are used. The solid lines are calculated torque curves according to Eq. (10) and the literature value of $\eta_{Glycerol} = 2.8$ Pa s.

using the literature value for the viscosity of glycerol and the given geometry of the shear cell. The solid lines in Fig 7 do not represent fits to the experimental data but merely the expected torque based on the above calculation of the flow field. Good agreement between the torque data and the calculation confirms the validity of the no-slip boundary conditions and justifies the assumption of laminar flow for the present experiments. Effects due to the finite length of the cylinders have also been neglected.

The energy per unit time, P, which is dissipated inside the liquid, is equal to the rate of work that is performed by the inner, rotating cylinder:

$$P = -2\pi R_1 L u_\theta(R_1) s(R_1) = \frac{4\pi L R_1^2 R_2^2}{R_2^2 - R_1^2} \Omega^2 \eta \ . \tag{12}$$

Typical dimensions of the shear cell used for the BMG forming alloys are $R_1 = 11.11 \times 10^{-3}$ m, $R_2 = 12.70 \times 10^{-3}$ m, and $L = 35 \times 10^{-3}$ m. With a maximum angular frequency of 10 s^{-1}, the total power dissipated in the fluid with a viscosity of 10 Pa s is less than 0.12 J s^{-1}. If thermal conduction from the shear cell mount and the inert atmosphere is neglected, electromagnetic radiation from the graphite is the only means of establishing energy balance in the shear cell. With the power,

$$P_{\text{radiation}} = \sigma_{\text{S.B.}} \varepsilon A T^4, \tag{13}$$

emitted from the cell, an energy increase of 0.1 J per second yields a temperature rise of the apparatus of about 0.2 K with the above parameters. This can be neglected compared to thermal gradients inside the shear cell of about ±4 K. In Eq. (13), $\sigma_{\text{S.B.}} = 5.670 \times 10^{-8}$ J s^{-1} m^{-2} K^{-4} is the Stefan-Boltzmann constant, ε the total hemispherical emissivity of the graphite, and A, the total outer area of the shear cell.

2.3. Graphite as a Crucible Material

The crucible material used in the construction of the concentric cylinder shear cell has to fulfill several requirements in order to be used in conjunction with Zr-based metallic liquids. The no-slip boundary conditions described in chapter 2.2 require an intimate contact between the liquid and the crucible walls. In most applications involving liquid metals it is not desirable that the liquid wets the container. However, wetting between the shear cell and the liquid is a prerequisite for the present viscosity measurements. At elevated temperatures reactions between the metallic liquid and the crucible material are therefore of concern.

The wetting of V1 on the graphite is shown in the photograph and the schematic in Fig 8. The sample, processed in the liquid at 1300 K for 12 min, shows a wetting angle of ca. 3° on the crucible interface. A high vacuum anneal of the graphite at a temperature of 1300 K was employed prior to the experiment. In Fig 8, a ca. 0.5 mm deep zone within the porous graphite, where the metallic liquid has penetrated the crucible wall, is visible. The schematic demonstrates that the penetration of the liquid into the graphite serves as a precursor for macroscopic wetting on the porous surface. In this process, the microscopic contact angle between the liquid and the non-porous substrate can be significantly larger than zero.

Scanning electron microscopy analysis has shown that a Zr-C reaction layer with a width of ca. 0.5 μm forms between the graphite and V1. Therefore, upon penetrating the porous structure, the liquid's composition will drift to a composition with less favorable glass forming ability. The changed composition of the alloy is

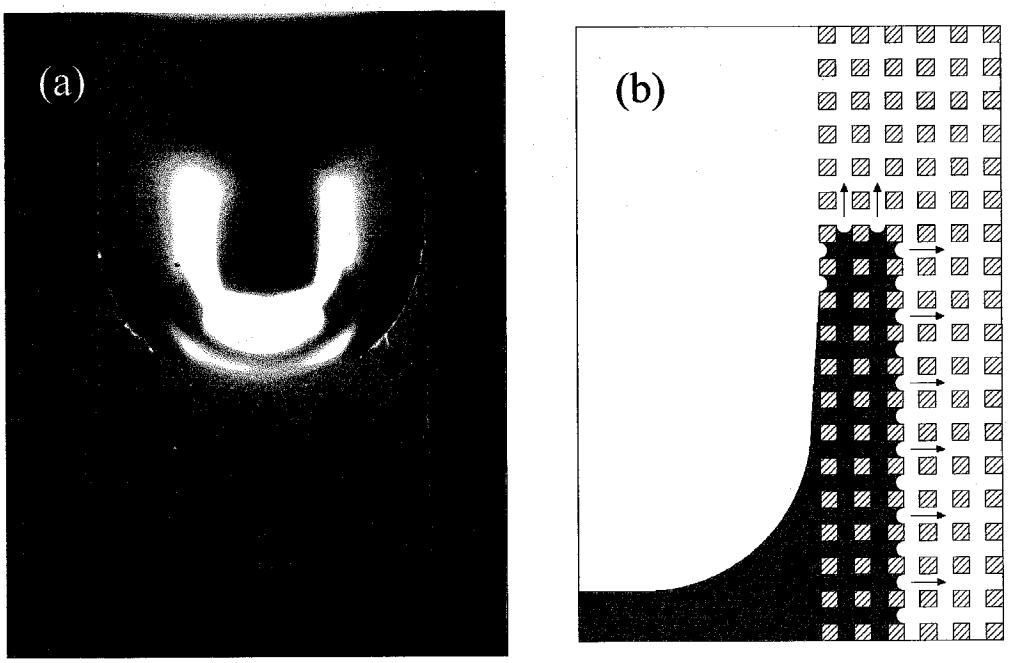

Fig. 8 Photograph and schematic of the liquid–graphite interface

(a) Photograph of the cross section of a cylindrical graphite crucible containing 480 mg of V1. The liquid has infiltrated the porous graphite up to a depth of ca. 0.5 mm. (b) The schematic illustrates (in two dimensions) the wetting of a liquid on a porous substance.

likely to correspond to a higher liquidus temperature and the flow of the liquid inside the porous graphite will eventually be limited by crystallization at the penetration front for a given processing temperature.

2.4. Capillary Flow Rheometry

Most of the viscosity measurements for a variety of liquids at or near room temperature have been performed with capillary tube viscometers. In these experiments, the liquid flows under the influence of a pressure gradient from one reservoir through a capillary into a second reservoir. For laminar flow of a Newtonian liquid and no-slip boundary conditions at the capillary wall, the volume flow rate, $\Delta V/\Delta t$, through the capillary is inversely proportional to the liquid's viscosity (Hagen-Poiseuille law [12]):

$$\frac{\Delta V}{\Delta t} = \frac{\pi R_{cap}^4}{8\eta}\frac{\Delta p}{\Delta l}. \tag{14}$$

The pressure gradient, Δp, is measured along the length, Δl, of the capillary having an inner radius R_{cap}.

In Fig 9 a schematic of the setup used for the capillary flow studies of metallic liquids in this work is shown. An ingot of ca. 40 g of the alloy is melted inside an inductively heated cylindrical graphite crucible. The capillary is inserted vertically into the melt and subsequently the pressure of the Ar atmosphere is increased. The liquid flows with a rate, $\Delta V/\Delta t$, into the upper reservoir. The upper part of the graphite crucible is equipped with a 1.5 mm wide slit that allows for the observation of the height, h, of the liquid inside the upper reservoir. A motor driven single lens reflex

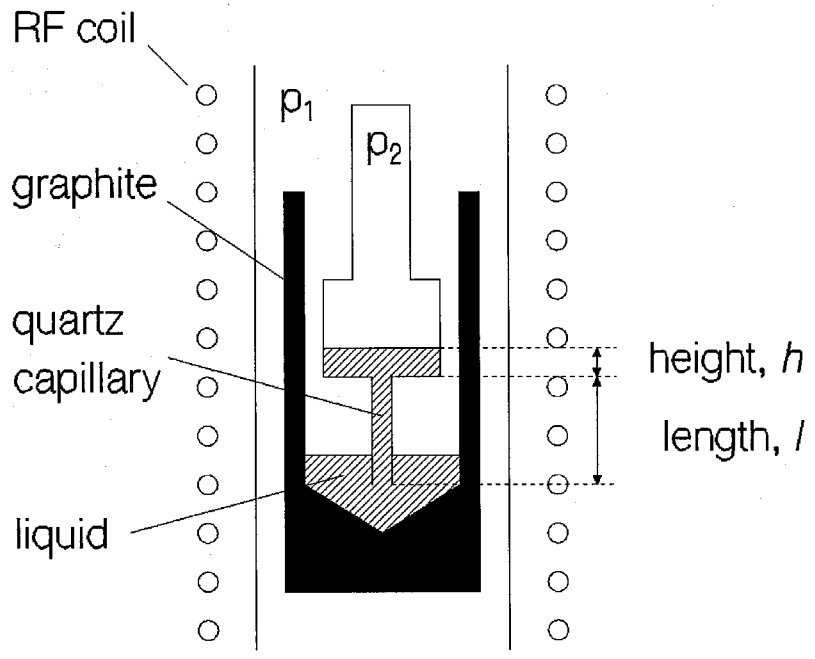

Fig. 9 Capillary flow rheometry

Schematic setup to measure the flow rate of a liquid through a quartz capillary at elevated temperatures. The liquid is contained in an inductively heated graphite crucible. Along the length, l, of the capillary, a pressure gradient, $\Delta p = p_1 - p_2$, is established through an Ar atmosphere. The increase in height within the upper reservoir with time is monitored with a motor-driven SLR camera.

(SLR) camera photographs the momentary height at intervals of 2.52 s. The volume flow rate,

$$\frac{\Delta V}{\Delta t} = \pi R_{\text{res}}^2 \frac{\Delta h}{\Delta t}, \tag{15}$$

can be determined from the increase in height, $\Delta h/\Delta t$, of the liquid column inside the upper cylindrical reservoir with diameter, R_{res}. Consequently, the viscosity can be determined from a measurement of $h(t)$ by:

$$\eta = \frac{R_{\text{cap}}^4}{8 R_{\text{res}}^2} \frac{\Delta p}{\Delta l} \left(\frac{\Delta h}{\Delta t} \right)^{-1}. \tag{16}$$

A type K thermocouple inserted into the crucible wall measures the temperature of the graphite crucible. For the case of a vertical capillary, corrections to Eq. (14) can be applied to account for the finite size of the reservoirs, i.e., for a time dependent pressure gradient per length, $\Delta p/\Delta l$ [13].

3. VISCOUS FLOW OF ZR-BASED GLASS FORMING ALLOYS

Recently, viscosity measurements [14, 15, 16, 17, 18] in the deeply supercooled liquid of multicomponent bulk metallic glass (BMG) forming alloys have found considerable attention. Beam bending and parallel plate rheometry are useful techniques for studying the flow of deeply supercooled samples in the viscinity of the glass transition regime. For those measurements, the material is first quenched into the amorphous state and then heated to temperatures where the equilibrium viscosity of the supercooled liquid can be studied within typical timescales of some 10 seconds to several hours [16]. Even for the most stable amorphous metallic alloys, the onset of crystallization limits the experimentally accessible temperature range of the supercooled liquid to about 100 K [14, 19]. Relatively few data are available from high temperature rheometry in the equilibrium liquid or slightly supercooled liquid state of metallic systems [18, 20, 21].

In chapter 3.1 experimental results from the concentric cylinder viscometer and from capillary flow will be presented. In the following analysis, the high temperature limit of the viscosity of the liquid will play an important role. For this reason, in chapter 3.2 the rate theory of flow will be revisited for the limiting case of high temperatures. The concept of classifying liquids according to their fragility follows from this high temperature limit of the viscosity. The viscosity of V1 is analyzed according to the entropy and free volume model of flow in chapters 3.3 and 3.4, respectively. Published heat capacity data and specific volume measurements

complement the discussion and allow for a detailed comparison of the two phenomenological models.

3.1. Viscosity: Experimental Results

Typical torque readings from a concentric cylinder shear cell containing liquid V1 are shown in Fig 10. The inner cylinder is alternately rotated in clockwise and counterclockwise direction for 60 s each. In this way, determination of the torque baseline is straightforward and the resolution of the viscosity measurement is doubled compared to simple continuous motion. The torque meter signal (mV) is converted via the calibration curve of Fig 6 and Eq. (11) into a torque reading (Nm). Analysis of the flow field between the two cylinders from chapter 2.2, which resulted in Eq. (10) yields the viscosity, η, as a function of the temperature. The decrease in the torque signal with increasing temperature in Fig 10 arises from the decrease in viscosity of the liquid alloy. The resolution of the torque sensor in conjunction with the increasing electrical noise from the RF heating coil does not allow for viscosity measurements in excess of 1200 K for the present system.

The viscosity of the supercooled liquid state of V1 was also measured upon cooling into the supercooled liquid state. The measured viscosity as a function of temperature for various shear rates is plotted in Fig 11. No dependence of the viscosity on shear rate is observed indicating Newtonian flow behavior for the present temperature range and the shear rates indicated in Fig 11. The sharp increase in the viscosity signal in Fig 11, representing the onset of solidification, will be discussed in chapter 5.2.

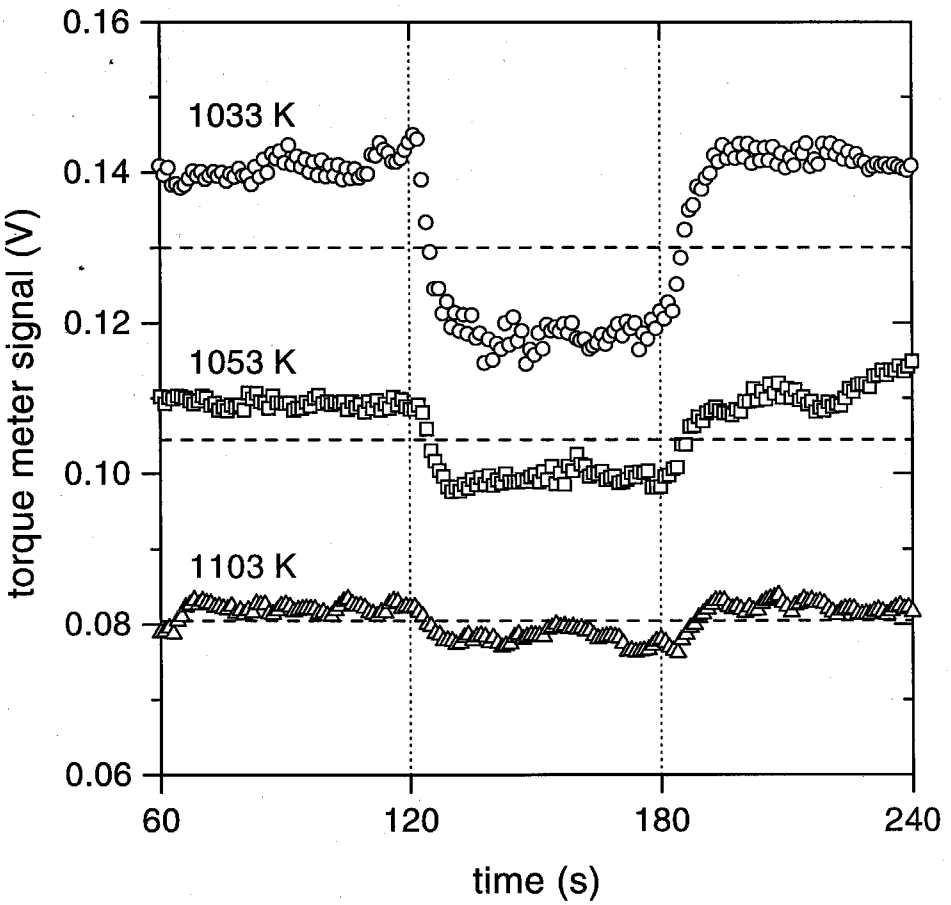

Fig. 10 Isothermal torque reading at constant shear rate

Clockwise and counterclockwise rotation of the inner cylinder for 60 s results in an alternating torque signal. The temperature is raised in steps of 50 K and the system is held at each temperature for 180 s prior to each experiment to allow for thermal equilibrium within the shear cell. The baselines (---) of the torque meter signals are shifted by arbitrary offsets.

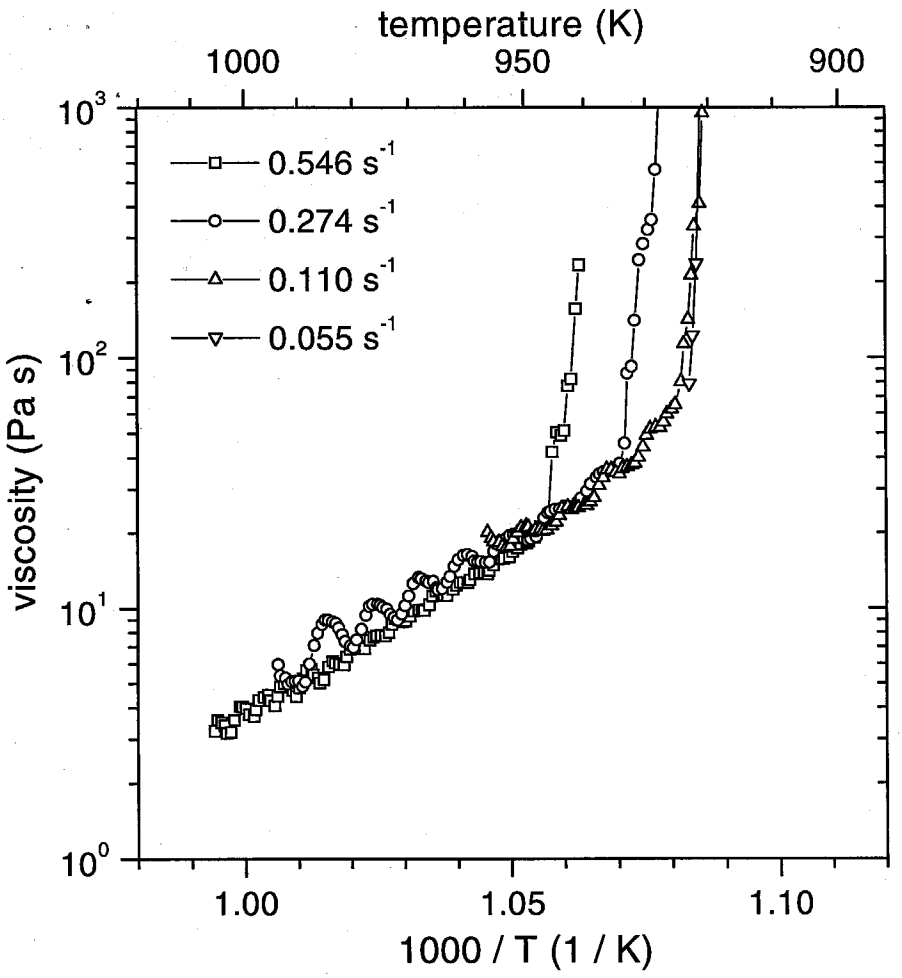

Fig. 11 Viscosity measurements upon linear cooling

Viscosities during linear cooling with a cooling rate of 0.66 K/s (see chapter 5.3). The average shear rates according to Eq. (7) are indicated.

Results from a typical capillary flow experiment of the equilibrium liquid of V1 are shown in Fig 12. The height of the liquid in the upper reservoir (see Fig 9) is determined from the image analysis of 35 mm slides taken by a motor driven SLR camera. The time interval between two frames is 2.52 s. Consequently, Eq. (16) yields the viscosity of the liquid.

In Fig 13 the present high temperature viscosity measurements are plotted in conjunction with published results for several metallic elements [22] and for metallic glass forming systems [18, 21, 23]. The viscosity of V1 at its liquidus temperature is about 3 orders of magnitude larger compared to metallic elements at their melting point. Extrapolating the viscosity of V1 to higher temperatures in Fig 14 according to the free volume model (see chapter 3.4), one finds a 'normal' melt viscosity for a metallic system at about the average melting point of V1's constituents. An extrapolation of the viscosity curve of Ni is also plotted to guide the eye. The comparison to a so-called fragile liquid (see chapter 3.2) like Ni shows that it is the proximity of V1's composition to a deep eutectic in conjunction with strong liquid behavior that lead to sluggish kinetics in the equilibrium melt.

3.2. High Temperature Limit of the Viscosity

In this chapter, Eyring's concept of rate theory [24] is applied towards the high temperature limit of the viscosity of the liquid state. For that purpose, the liquid is envisaged to be stable in the limit $T \rightarrow \infty$, i.e., no phase transformation to the gaseous state occurs. The temperature dependence of the density or of a typical inter-atomic length, a, is neglected to keep the liquid in the condensed state.

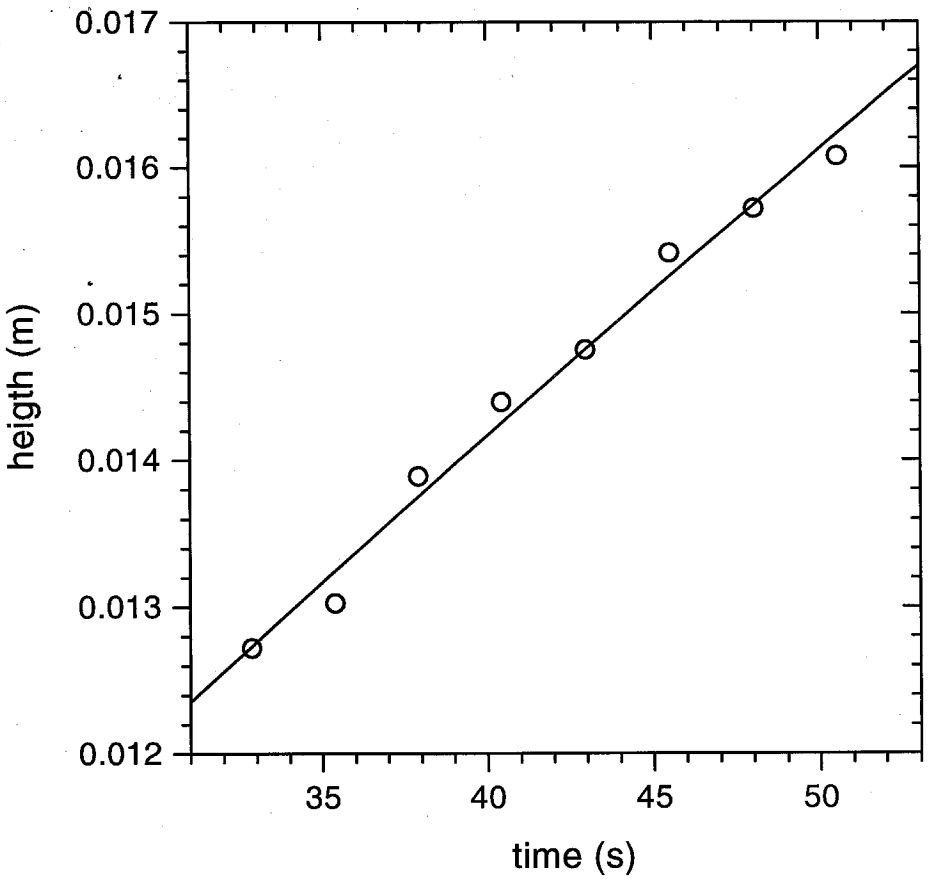

Fig. 12 Capillary flow rheometry: experimental results

Height, h, of the liquid inside the upper reservoir as obtained by image analysis of photographs taken at 2.52 s intervals. A setup according to Fig. 9 with $R_{cap} = 1.0 \times 10^{-3}\ m$, $R_{res} = 1.5 \times 10^{-2}\ m$, $\Delta p = 6800\ Pa$, *and* $\Delta l = 1.73 \times 10^{-2}\ m$ *was used. The viscosity, according to Eq. (16), is* $\eta = 4.4\ Pa\ s$.

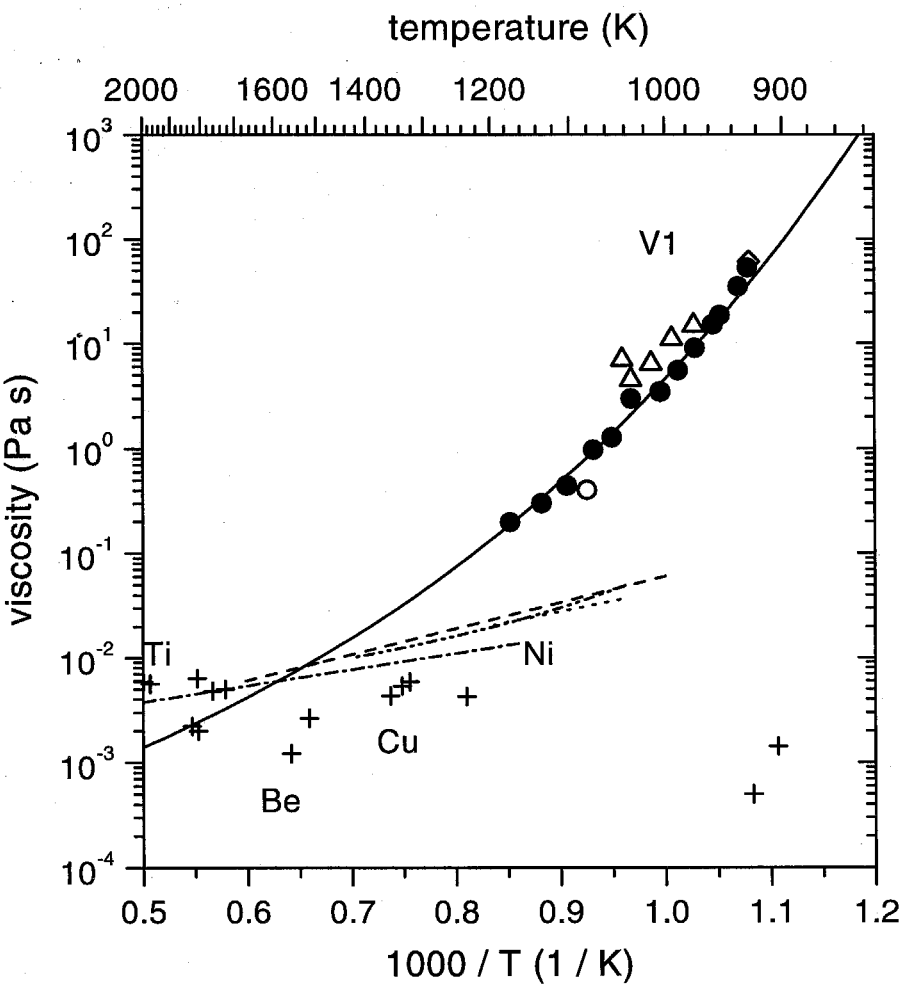

Fig. 13 Viscosities of liquid metals at high temperatures

Results from viscosity measurements of V1 obtained by the rotating cup viscometer (•) and the capillary method (△) as well as a Cohen-Grest fit (—). Data for $Pd_{78}Cu_6Si_{16}$ (·····) [18], $Pd_{82}Si_{18}$ (---) [21], $Ti_{34}Zr_{11}Cu_{47}Ni_8$ (···) [23], and the viscosities of several metallic elements at their melting points (+), see Fig. 14, are plotted for comparison. The viscosity of Ni is extrapolated into its supercooled liquid state (·····).

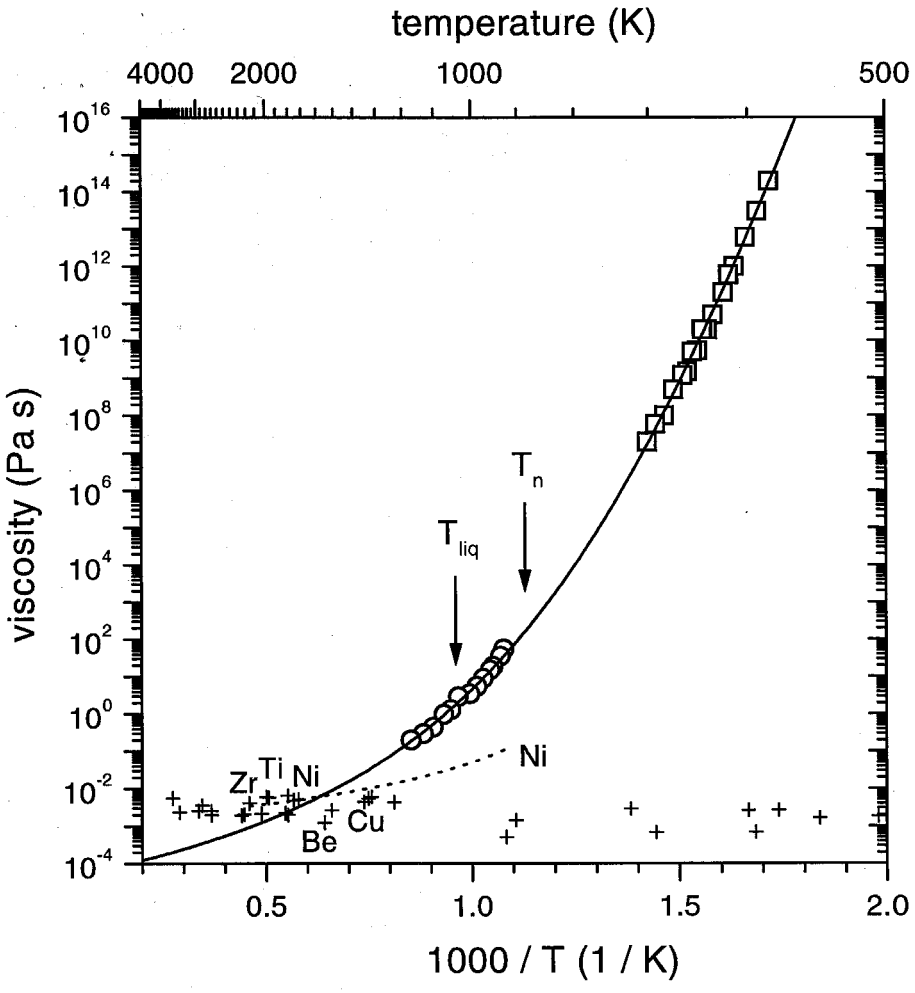

Fig. 14 Arrhenius plot of the viscosity of V1 and metallic elements

Viscosity of V1 as measured by beam bending (□) and concentric cylinder rheometry (○) as well as a Cohen-Grest fit (—), Eq. (32), Eq. (36). Melt viscosities (+) of Sn, Bi, Tl, Cd, Pb, Zn, Te, Sb, Mg, Ag, Ac, Au, Cu, Mn, Be, Ni, Co, Fe, Sc, Pd, V, Ti, Pt, Zr, Cr, Rh, B, Ru, Ir, Mo, Os, Re, and W near their melting point (in order of increasing melting point) [22] and an extrapolation of the viscosity of Ni (···) into its supercooled liquid state.

A shear strain rate, $\dot{\gamma}$, is then applied to the material resulting in a macroscopic shear stress $s = \eta\dot{\gamma}$. It is assumed that at sufficiently high temperature viscous flow is controlled by single particle motion, i.e., the shear strain rate is homogeneous down to distances on the order of an interatomic length a,

$$s = \eta_0 \frac{\Delta u}{a}, \tag{17}$$

where the velocity difference, Δu, per length a is measured perpendicular to the direction of flow. The rates, k_f and k_b, of atoms moving forward and backward in the direction of flow under the presence of the shear stress,

$$k_f = k_0 \exp\left(-\frac{-\frac{1}{2}sa^3}{kT}\right) \text{ and } k_b = k_0 \exp\left(-\frac{+\frac{1}{2}sa^3}{kT}\right), \tag{18}$$

are written according to Eyring. In Eq. (18), the effect of the shear stress is to create a potential energy gradient, sa^3, per inter-atomic length, a, that favors forward compared to backward motion. Consequently, the velocity gradient can be written as the difference between the two rates, multiplied by the average displacement, a:

$$\Delta u = (k_f - k_b)a = 2k_0 a \sinh\left(-\frac{sa^3}{2kT}\right). \tag{19}$$

In the limit of high temperatures, $kT \gg sa^3$, the first term of a Taylor series yields:

$$\lim_{T\to\infty} \Delta u = \frac{k_0 sa^4}{kT}, \tag{20}$$

while solving for the viscosity coefficient in Eq. (17) results in:

$$\eta = \frac{kT}{k_0 a^3}. \tag{21}$$

Eyring found a universal expression for the rate constant, k_0, from the frequency, $\bar{v}/a$ (average velocity per length), times the one-dimensional translational partition function, f_{tr}:

$$k_0 = f_{tr}\frac{\bar{v}}{a} = \frac{\sqrt{2\pi m^* kT}}{h}\bar{v}. \tag{22}$$

The average velocity,

$$\bar{v} = \sqrt{\frac{kT}{2\pi m^*}}, \tag{23}$$

results from the thermal energy per degree of freedom and leads to:

$$k_0 = \frac{kT}{h}. \tag{24}$$

Finally, Eq. (24) inserted in Eq. (21), with $v_m = a^3$ as the average atomic volume, results in a universal expression for the high temperature limit of the viscosity of the liquid state:

$$\eta_0 = \frac{h}{v_m}. \tag{25}$$

For the present system, V1, the atomic volume, $v_m = M/(N_A \rho)$, can be derived from specific volume measurements [25] that yielded a density, ρ, of about $6\,\mathrm{g\,cm^{-3}}$ for the liquid. The average molar mass, M, amounts to $60\,\mathrm{g\,g\text{-}atom^{-1}}$ and N_A is Avogadro's number. With this, Eq. (25) leads to a lower limit of the viscosity of Vit1 of $\eta_0 = 4\times10^{-5}\,\mathrm{Pa\,s}$.

The classification of liquids according to various degrees of 'fragility', made popular by Angell [26], relies on the applicability of Eq. (25) for a wide range of liquids. The specific volume is known to vary by only about one order of magnitude between different liquids. Therefore, the high temperature limit of the viscosity is always on the order of 10^{-5} to 10^{-4} Pa s.

Scaling the viscosity-temperature curves to an (arbitrary) viscosity of 10^{12} Pa s results in the normalized Arrhenius plot as shown in Fig 15. All curves meet – by the above definition of T_g – at 10^{12} Pa s (or 10^{13} Poise). So-called 'strong' liquids, like SiO_2, exhibit an Arrhenius-like temperature dependence. The viscosity of 'fragile' liquids has a stronger temperature dependence in the vicinity of T_g and a weaker temperature dependence at high temperatures.

The viscosities of V1 and $Zr_{46.75}Ti_{8.25}Cu_{7.5}Ni_{10}Be_{27.5}$ (V4) [14] indicate that these liquids are less fragile than other metallic melts [27]. The difference in the specific heat capacity between the amorphous and the supercooled liquid state in the glass transition regime is another measure of the fragility of a system. Again, the bulk metallic glass forming alloys V1 and V4 are strong liquids compared to normal metallic melts.

3.3. Entropy Model for Viscous Flow

The kinetic slowdown reflected in the increase in viscosity with decreasing temperature can be connected to the thermodynamic functions of the supercooled liquid through the so-called entropy model for viscous flow. For a variety of systems, it has been found [26] that with an increase in viscosity the isobaric entropy decreases

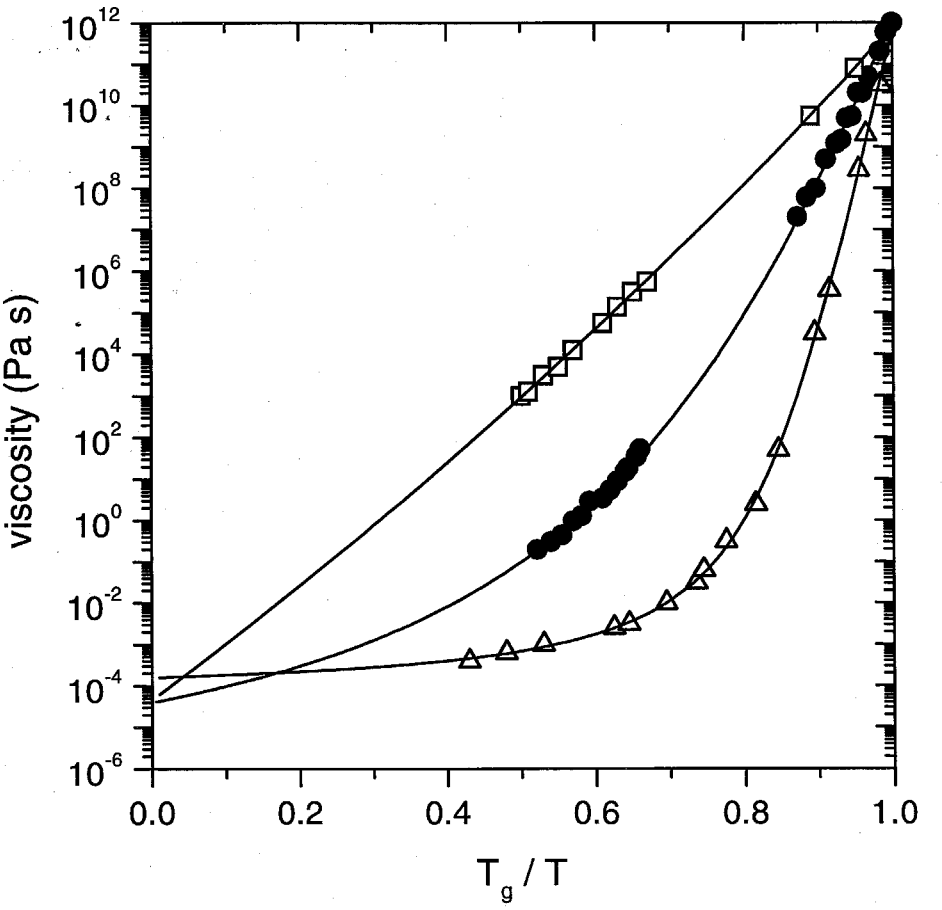

Fig. 15 Normalized Arrhenius plot of the viscosity of glass forming systems

The inverse temperature, 1/T, is normalized to the glass transition temperature, T_g, which is defined for this plot as the temperature where the viscosity reaches a value of 10^{12} Pa s. The viscosity of V1 (•) is plotted in comparison with a strong liquid, SiO_2 (□), and a fragile liquid, o-terphenyl (△) [2].

relatively sharply in the deeply supercooled melt. Adam and Gibbs [28] developed a theory on cooperative relaxation in liquids and supercooled liquids that quantifies the dependence of transport properties like the viscosity on the entropy of the system. The increase in relaxation times and viscosity with increasing supercooling is directly linked to a decrease in configurational entropy, S_c, of the system. Within this model, the viscosity is expressed as

$$\eta = \eta_0 \exp\left(\frac{C}{TS_c}\right), \tag{26}$$

where the constant C represents an effective free enthalpy barrier for cooperative rearrangements. The pre-factor, η_0, in Eq. (26) can be calculated according to Eq. (25) to be $4 \cdot 10^{-5}$ Pa s. It is further assumed that the vibration of the atoms in a (supercooled) liquid is modified only by a slight anharmonicity compared to vibrations in the crystalline state. Neglecting this difference, the configurational entropy can therefore be approximated by the difference, ΔS, between the total entropies of the liquid and the crystal,

$$S_c \cong S_{\text{liq.}} - S_{\text{cryst.}}, \tag{27}$$

assuming that their vibrational parts of the entropy are equal. One should note, however, that in a multicomponent system like V1, the 'crystalline state' is composed of a variety of crystalline phases each with a certain homogeneity range with respect to its composition. Except for one-component systems or simple alloys where the structure of the equilibrium phases and their respective compositions are known, the entropy, $S_{\text{cryst.}}$, is in practice treated as a phenomenological quantity. In this spirit, ΔS

results from an integration of the measured heat capacity difference $\Delta c_p = c_{p,liq} - c_{p,xtl}$ between the liquid and the crystal [29]:

$$S_c = S_c(T_{liq}) - \int_{T}^{T_{liq}} \frac{\Delta c_p}{\tilde{T}} d\tilde{T} . \qquad (28)$$

Inserting Eq. (28) in Eq. (26), the configurational entropy at the liquidus, $S_c(T_{liq})$, is treated as a fitting parameter. This takes into account that in a multicomponent system the crystalline state can have a considerable amount of entropy of mixing. In fact, a disordered solid solution can have a larger entropy of mixing than the supercooled liquid of the same composition with strong tendency to topological and chemical short range order [30].

If the specific heat capacity difference is proportional to the inverse temperature, i.e., if $\Delta c_p \sim 1/T$, Eq. (26) in conjunction with Eq. (28) is formally equivalent to a Vogel-Fulcher-Tammann (VFT) relation:

$$\eta = \eta_0 \exp\left(\frac{B}{T - T_0}\right). \qquad (29)$$

For the present alloy, however, a $1/T$ dependence clearly underestimates the temperature dependence of Δc_p as shown in Fig 16. Consequently, a quantitative analysis of the flow behavior of Vit1 by a VFT relation cannot be justified on the basis of the Adam-Gibbs entropy model. In Fig 16, the low temperature part of the heat capacity (dashed curve) was calculated according to the Debye model with an estimated T_{Debye} = 305 K in analogy to V4.

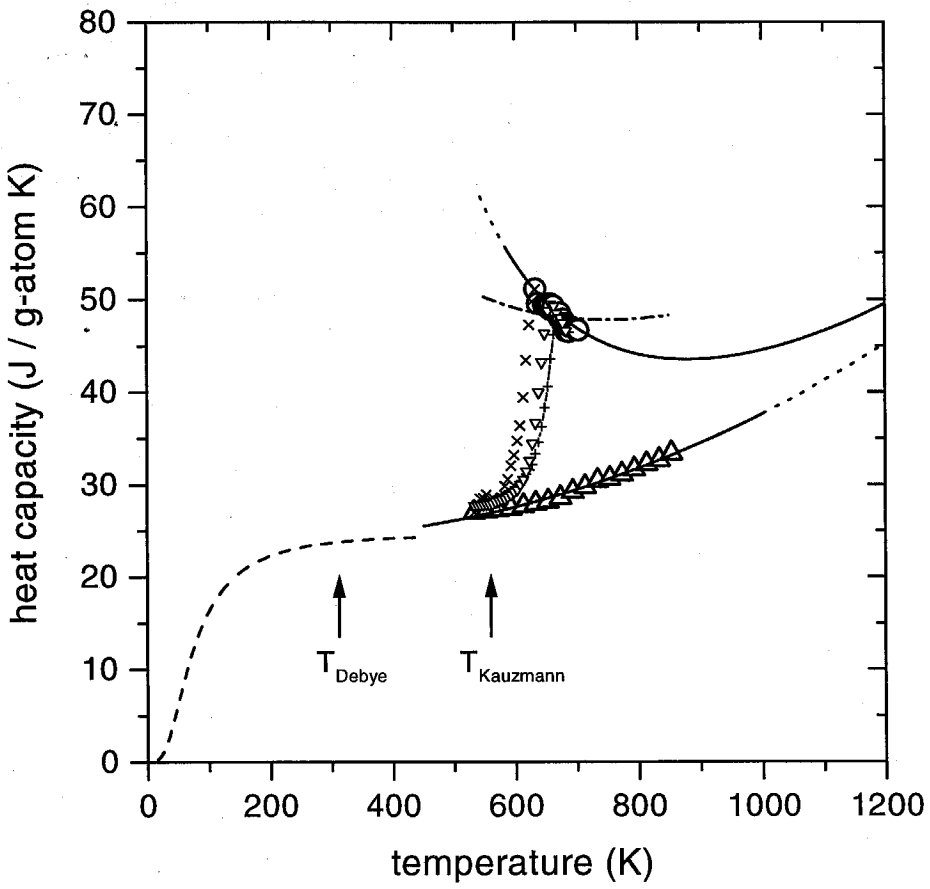

Fig. 16 Specific heat capacity

Specific heat capacities of V1 in the liquid (○) and crystalline (△) state. Equation (30) and Eq. (31) are shown as solid curves (—). The measured heat capacity during the calorimetric glass transition is shown for various heating rates (×, ▽, +) [29]. The low temperature part of the heat capacity (---) was calculated according to the Debye model with an estimated T_{Debye} = 305 K. A $\Delta c_p \sim 1/T$ least squares fit to the specific heat capacity of the supercooled liquid is indicated (- · -).

In order to comply with the high temperature limit of the viscosity according to chapter 3.2, the specific heat capacity difference in Eq. (28) has to vanish for $T \to \infty$. To avoid the condition $\Delta c_p = 0$ for finite T, i.e., to avoid a minimum in the viscosity, the following analytical expressions are used to fit the experimental specific heat measurements:

$$c_{p,xtl} = 3R + \beta_1 T + \beta_2 T^2, \tag{30}$$

$$c_{p,liq} = c_{p,xtl} + \beta_3 T^{-2} + \beta_4 T^{-3}. \tag{31}$$

From a least-squares fit of Eq. (30) and Eq. (31) to the experimental data, the parameters are (in SI units) $R = 8.314$, $\beta_1 = -8.021 \cdot 10^{-3}$, $\beta_2 = 2.076 \cdot 10^{-5}$, $\beta_3 = 2.940 \cdot 10^{6}$, and $\beta_4 = 3.934 \cdot 10^{9}$. They describe the experimental data very well (Fig 16) and yield a finite high temperature limit η_0 for the viscosity. Kubaschewski's formula [29] describes the heat capacity data equally well, but fails to comply with $\lim_{T\to\infty} \Delta c_p = 0$ and therefore with $\lim_{T\to\infty} \eta(T) = \eta_0$.

A fit of Eq. (26) to the viscosity data of V1 yields the two fit parameters $C = 203$ kJ g-atom^{-1} (or 2.1 eV atom^{-1}) and $S_c^{liq} = 15.8$ J K^{-1}g-atom^{-1}. The corresponding viscosity curve is shown in Fig 17, in comparison to results from the free volume model, which is discussed in chapter 3.3. Results obtained from the high temperature Couette viscometer as well as from beam bending rheometry [16] of V1 are included in Fig 17. Qualitative agreement between the measured viscosity and the entropy model is found, but, e.g., the tendency of the viscosity values to show Arrhenius behavior at temperatures below ca. 700 K is not entirely accounted for in Eq. (29).

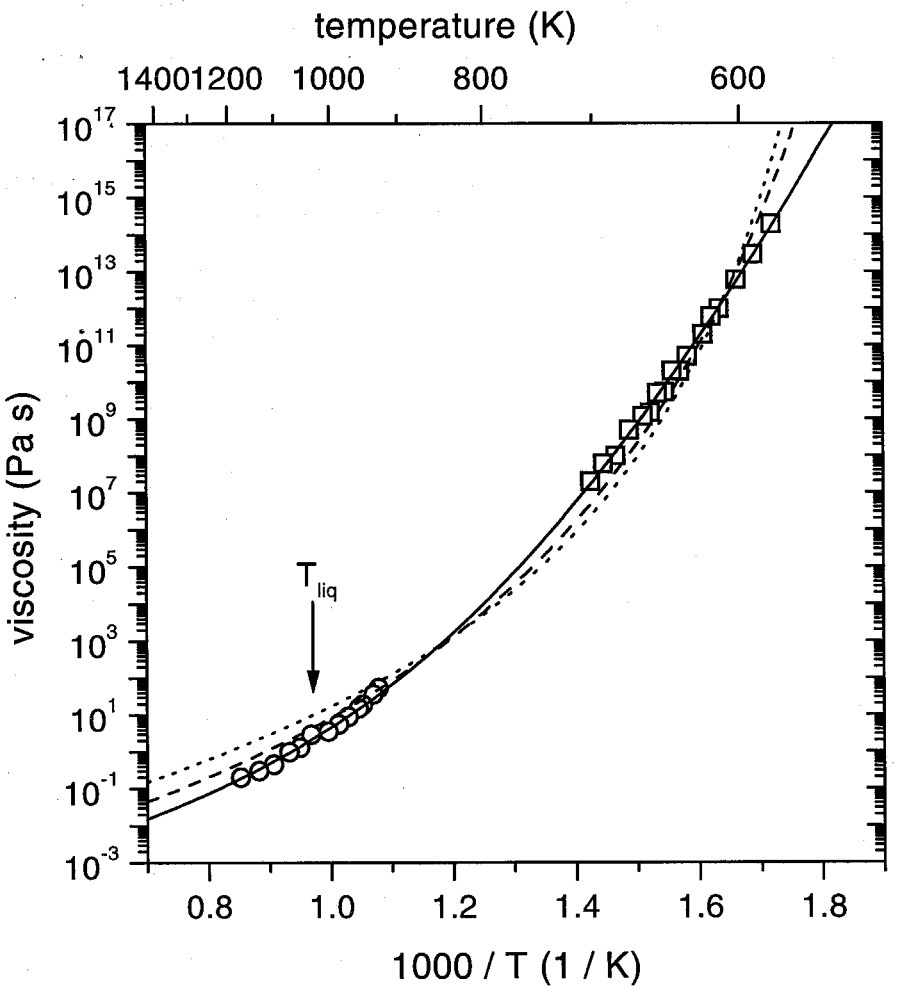

Fig. 17 Viscosity of V1 and least-squares fits of entropy and free volume model

Viscosity of V1 as measured by beam bending (□) and concentric cylinder rheometry (○). The data are fitted to the entropy model (···), Eq. (26), and the free volume model. The dashed curve (---) represents a VFT fit and the solid curve (—) a Cohen-Grest fit (see chapter 3.4).

Using the fit parameters C and S_c^{liq} and Eq. (26) to solve for the configurational entropy, we obtain Fig 18. The data points in Fig 18 result from the individual viscosity measurements converted via Eq. (26) into configurational entropies and the solid line is the configurational entropy according to the best fit of the viscosity data. Although the temperature dependence of the viscosity in Fig 17 is in qualitative agreement with Adam's and Gibb's theory, it is clear from Fig 18 that the decrease in entropy with supercooling cannot quantitatively account for the exact form of $\eta(T)$.

3.4. Free Volume Model for Viscous Flow

Within the free volume model, viscous flow in a liquid occurs as a consequence of density fluctuations or rearrangements of so-called free volume. It is essential to the theory that the atomic rearrangements take place spontaneously, i.e., without appreciable activation energy compared to kT. In this model, fluid motion in the liquid and supercooled liquid can occur, because in localized regions of configuration space, the free energy landscape of the atoms is flat compared to the thermal energy, kT. The amount of free volume in the supercooled liquid decreases with decreasing temperature and can eventually lead to structural arrest. The viscosity can be expressed as

$$\eta = \eta_0 \exp\left(\frac{b v_m}{v_f}\right) \tag{32}$$

with v_f as the average free volume per atom and $b v_m$ as the critical volume for flow [31]. The atomic volume v_m of V1 was measured by Ohsaka et al. [25] in levitation experiments to be $1.67 \times 10^{-29}\,m^3$ near the liquidus. The pre-factor $\eta_0 = h / v_m$ in

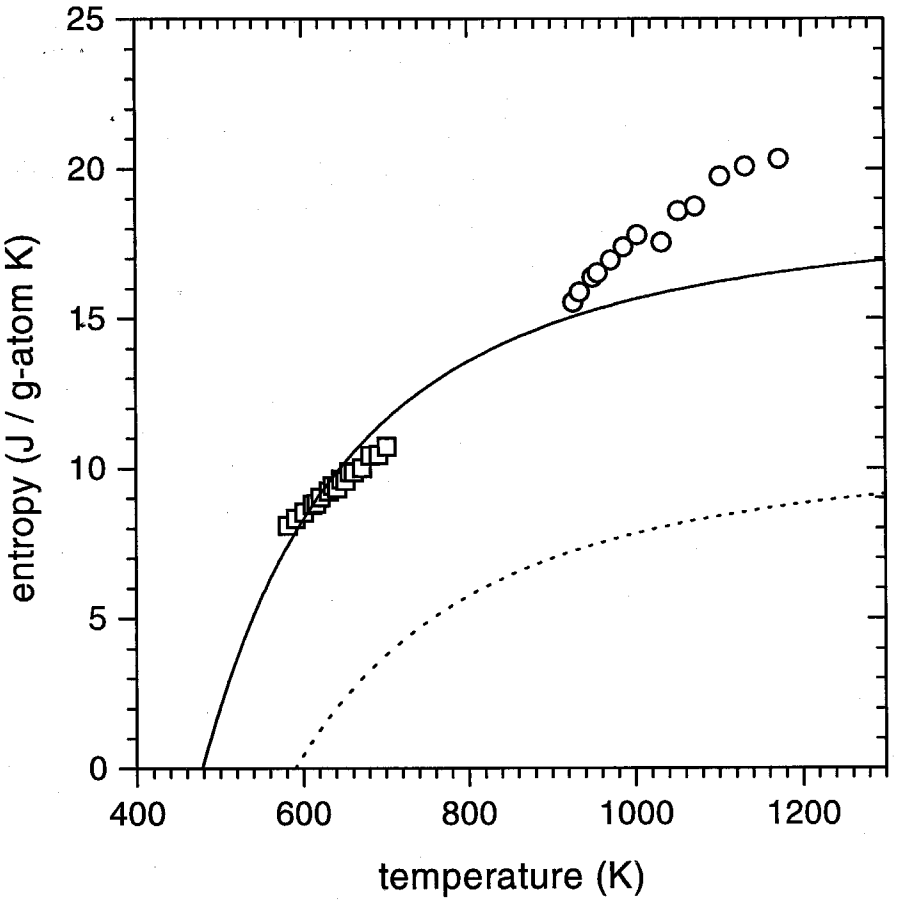

Fig. 18 Configurational entropy of V1

Entropy difference between the liquid and the crystalline state of V1 (···) and configurational entropy, S_c, (—) of the liquid as obtained from a fit of Eq. (26) to the viscosity data in Fig. 17. The viscosity data are converted via Eq. (26) into configurational entropies, S_c (○), (□).

Eq. (32) is set to 4×10^{-5} Pa s as discussed in chapter 3.2. Under the assumption of a linear relation,

$$v_f = v_m \alpha_f (T - T_0), \tag{33}$$

between the free volume and the temperature, Eq. (32) takes the form of a VFT equation:

$$\eta = \eta_0 \exp\left[\frac{b}{\alpha_f (T - T_0)}\right]. \tag{34}$$

Here, α_f characterizes the increase in free volume with temperature. Often, the dimensionless parameter

$$D_* = \frac{b}{\alpha_f T_0} \tag{35}$$

is introduced in Eq. (34), to classify a liquid according to its fragility [26, 32]. At the temperature T_0, the free volume vanishes and viscous flow is no longer possible, according to this model. The so-called VFT temperature, T_0, is usually treated as a fit parameter. For the V1 data, shown in Fig 14, one finds $D_* = 16.5$ and $T_0 = 426.3$ K. The present values of D_* and T_0 differ slightly from previously published results [24] due to the recent high temperature measurements of η in the equilibrium liquid and supercooled liquid. Compared to other metallic systems, the relatively high value of D_* reflects 'strong' liquid (see chapter 3.2). It has been demonstrated [27] that the glass forming ability of a metallic system represented by the critical cooling rate correlates with its fragility parameter D_*. The stronger the liquid (i.e., the higher D_*), the lower the critical cooling rate to bypass crystallization.

In an extended version of the free volume model proposed by Cohen and Grest [31], the free volume decreases to zero, only for $T = 0$, and the viscosity is expressed through a temperature-dependent free volume [31]

$$v_f = \frac{k}{2\varsigma_0}\left(T - T_0 + \sqrt{(T - T_0)^2 + \frac{4v_a\varsigma_0}{k}T}\right). \tag{36}$$

A least-squares fit of the logarithm of the viscosity data to Eq. (32) in conjunction with Eq. (36) describes the data very well as shown in Fig 14. The three fit parameters are found to be $bv_m\varsigma_0 / k = 4933$ K, $T_0 = 672$ K, and $4v_a\varsigma_0 / k = 162$ K. Cohen and Grest's concept of a volume dependent free energy for liquid- and solid-like cells, which led to Eq. (36) models the viscosity of V1 better than a Vogel-Fulcher-Tammann (VFT) relation as the comparison in Fig 14 shows.

In the limit of low temperatures, $T \to 0$, the free volume in Eq. (36) becomes proportional to the inverse temperature, $v_f \sim T^{-1}$. This corresponds to an Arrhenius-like temperature dependence of the viscosity in Eq. (32). In the limit of high temperatures, $T \to \infty$, Eq. (36) yields $v_f \sim (T - T_0)^{-1}$, corresponding to a VFT relation in Eq. (32). The transition region from $v_f \sim (T - T_0)^{-1}$ to $v_f \sim T^{-1}$, i.e., from VFT to Arrhenius behavior, is found to be around $T_0 = 672$ K.

From the viscosity measurements, the normalized free volume ratio, $v_f / (bv_m)$, in Eq. (32) can be calculated in conjunction with the above fit. Data corresponding to the present viscosity data of V1 are shown in Fig 19 (left axes). The high temperature viscosity data yield

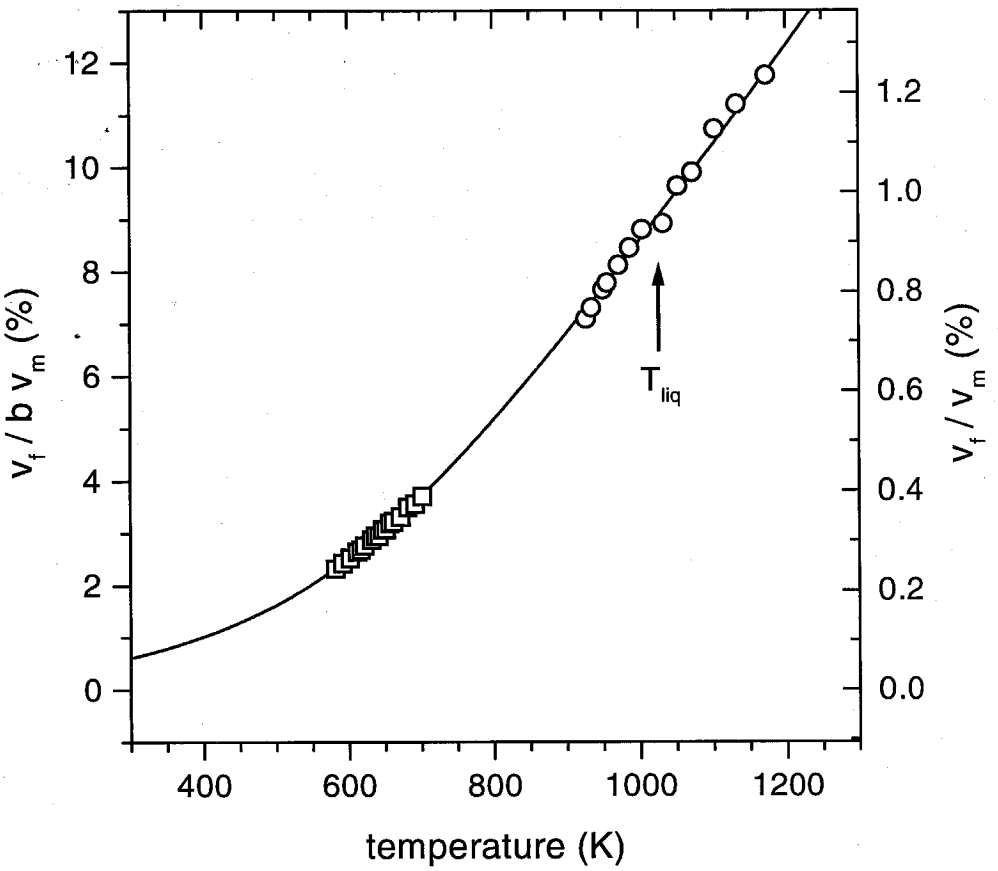

Fig. 19 Free volume of V1 as determined by the viscosity

Viscosity data from the concentric cylinder viscometer (○) and from beam bending (□) converted into relative free volume according to Eq. (32).

$$\frac{\alpha_f}{b} \equiv \frac{1}{bv_m}\frac{dv_f}{dT} = 1.83\times10^{-4}\ \mathrm{K}^{-1}, \tag{37}$$

with α_f as the average expansion coefficient for the free volume in the temperature range from 800 K to 1200 K. This increase in free volume with temperature can be approximated by the difference between the thermal expansion coefficients of the liquid and the glass [33],

$$\alpha_f = \alpha_{liq} - \alpha_{glass}, \tag{38}$$

with $\alpha_{liq} = 5.32\times10^{-5}\ \mathrm{K}^{-1}$ and $\alpha_{glass} = 3.39\times10^{-5}\ \mathrm{K}^{-1}$ [25]. From Eq. (37) and Eq. (38) the value of $b = 0.105$ can be calculated and the corresponding average free volume per atom, v_f / v_m, is shown in Fig 19 (right axes). At the liquidus temperature, one finds $v_f = 9.6\times10^{-3} v_m$, i.e., only about 1% of the sample's volume is 'free'. This small amount of free volume is consistent with the picture of a dense metallic liquid with slow kinetics.

The average interatomic spacing in liquid metals is – to a first approximation – determined by the size of the individual atoms. The latter may be calculated from the nearest neighbor distance in the crystalline state. In Fig 20 the specific volume of the liquid state, $v_{m,liq}$, to the 1/3 power is plotted as a function of the nearest neighbor distance, $a_{NN,xtl}$, in the crystalline state for a number of metallic elements [34]. The relation

$$\left(v_{m,liq}\right)^{\frac{1}{3}} = 0.925\, a_{NN,xtl} \tag{39}$$

describes the literature data of $v_{m,liq}$ and $a_{NN,xtl}$ to within ±4% as shown in Fig 20. Taking the weighted average of the nearest neighbor distances (atom diameters) of the

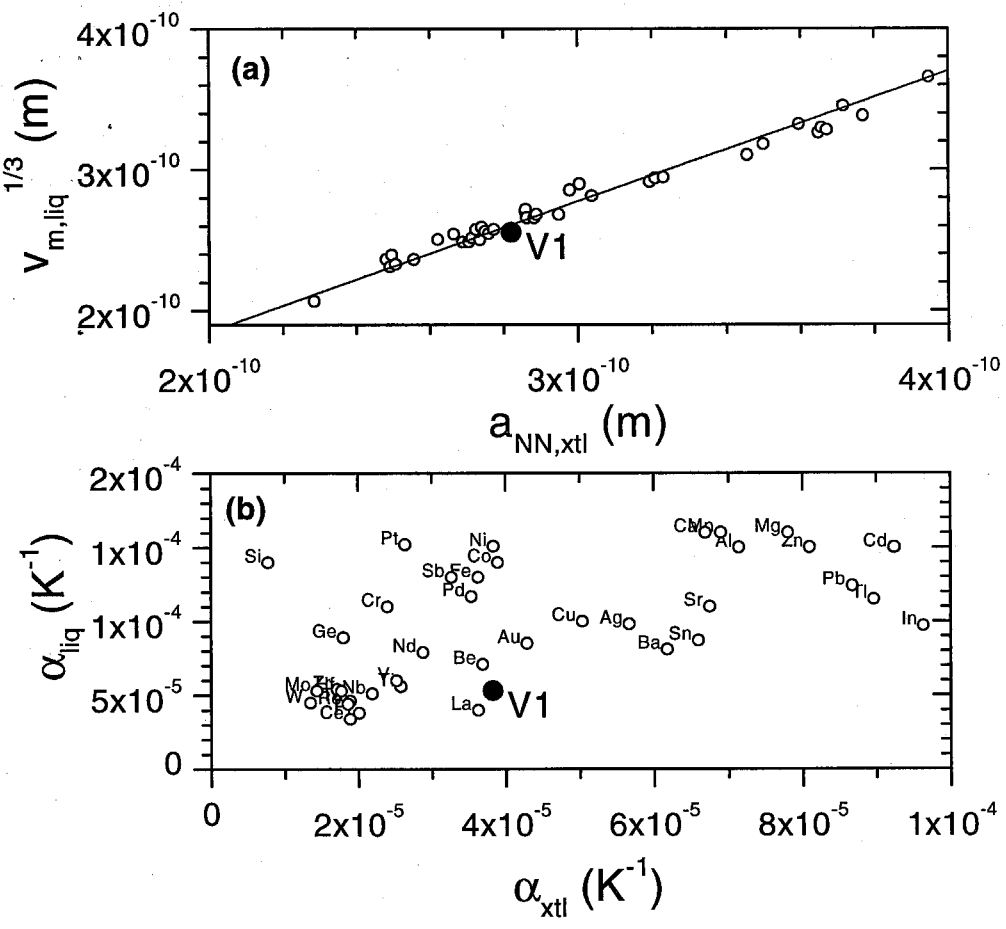

Fig. 20 Interatomic spacing and thermal expansion in liquids and crystals

(a) Average interatomic spacing as a function of the nearest neighbor distance in the liquid and crystalline state of V1 (•) and of the metallic elements Be, Fe, Ni, Cr, Co, Cu, V, Zn, Rh, Ru, Ir, Mo, Os, W, Pd, Re, Pt, Nb, Ta, Al, Au, Ag, Ti, Cd, Hg, Li, Hf, Mg, Zr, Tl, Pb, Th, Ce, Nd, Pr, Na, La, Ca, Sr, Ba, K, Rb, and Cs (◦) [34]. (b) Thermal expansion coefficient in the liquid [25] and crystalline state of V1 (•) and several metallic elements (◦) [22, 35].

elements, Zr, Ti, Cu, Ni, and Be, in the ratio of the atomic composition of V1, the specific volume of V1 in the liquid state is only slightly (2%) smaller than predicted by Eq. (39). In contrast, the thermal expansion coefficient, α_{liq}, of liquid V1 is considerably smaller than for most transition metals [35] as the comparison in Fig 20 (b) shows. The thermal expansion coefficient of the liquid enters through Eq. (38) into the fragility parameter, D_*, and a small α_{liq} is consistent with a large value of D_*, i.e., with strong liquid behavior.

As discussed in chapter 3.1 an extrapolating of the viscosity of V1 to higher temperatures in Fig 14 and Fig 17 according to the Cohen-Grest model, Eq. (32) and Eq. (36), yields a normal melt viscosity for a metallic system on the order of 10^{-3} Pa s at about the average melting point of V1's constituents [22]. For viscous flow one defines an apparent activation energy as

$$Q_\eta(T) = \frac{\partial(\ln\ \eta)}{\partial(1/kT)}, \tag{40}$$

which can be determined from the slope of the logarithm of the viscosity plotted versus inverse temperature. The apparent activation energies of V1 in the liquid and supercooled liquid state are plotted in Fig 21 in units of electron-volts and of the thermal energy, kT. The Cohen-Grest fit from Fig 17 was taken as a basis for calculating Q_η as defined in Eq. (40). At temperatures between 600 K and 650 K where the glass transition of V1 can be observed in conventional calorimetric experiments the apparent activation energy for viscous flow of the supercooled liquid is on the order of 4 eV. The finite low temperature limit of the apparent activation

energy In Fig 21 (a) represents the transition to an Arrhenius-like temperature dependence of the viscosity of V1 within the Cohen-Grest model.

The temperature dependence of the viscosity of the metallic elements in the experimentally accessible temperature range above the melting point is characterized by apparent activation energies, Q, of less than 0.5 eV. Similar to the viscosity itself (see Fig. 14), the apparent activation energy for viscous flow of V1 approaches normal values for a metallic system at about the average melting point of the constituents.

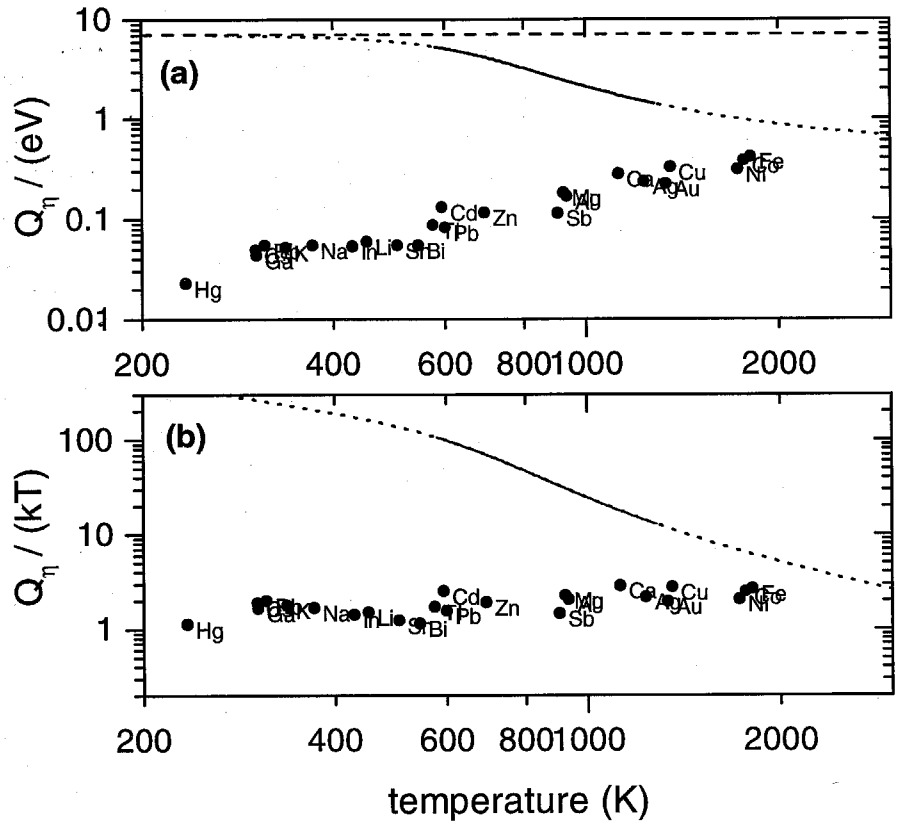

Fig. 21 Apparent activation energies for viscous flow

Apparent activation energies as calculated by Eq. (40) for V1 in units of eV and of kT. The solid parts of the curves (—) represent the experimentally accessible temperature range while the dotted parts (···) are extrapolations based on the Cohen-Grest model. For comparison, the measured apparent activation energies of several metallic elements are included (•) [22].

4. TIME SCALES IN THE LIQUID AND THE SUPERCOOLED LIQUID

4.1. Diffusion in the Liquid State

In order to quantify the time scale for atomic transport in the equilibrium melt, Au interdiffusion in liquid V1 was studied at 1050 K. Usually, the diffusion studies in liquid metals are complicated due to the influence of convection in the melt. Thermal gradients upon heating the sample to the diffusion temperature or unwanted thermal gradients during the isothermal anneal imply density gradients in the liquid that may trigger convective flow. In order to estimate the stability of the liquid against density driven convective flow, a spherical sub-volume with radius a of the liquid is considered. A buoyancy force,

$$F_b = \left(\frac{4}{3}\pi \rho a^3\right) g \alpha_{liq} \Delta T , \tag{41}$$

is exerted on the sub-volume if a temperature difference, ΔT, compared to the surrounding liquid exists. In Eq. (41), ρ is the density of the surrounding liquid, α_{liq} its thermal expansion coefficient, and g the gravitational constant. When the sub-volume has a velocity, U, relative to its surrounding, a frictional force,

$$F_f = 6\pi \eta a U , \tag{42}$$

according to Stoke's law will hinder its motion. The larger the viscosity, η, the larger the frictional forces that damp the convective flow. Under steady-state conditions, the time, (a/U), for the sub-volume to move a distance, a, will be on the order of the thermal diffusion time, $\left(C_p \rho a^2 / \kappa\right)$. If the frictional force is larger than the

buoyancy force, $F_f > F_b$, the system will be stable against density driven convective flow. Rearranging Eq. (41) and Eq. (42) leads to the stability criterion:

$$\frac{a^3 \rho^2 g C_p \alpha_{liq} \Delta T}{\eta \kappa} < \frac{9}{2}. \tag{43}$$

The radius of the diffusion crucible of 3×10^{-3} m serves as an upper limit for a. The density, ρ, of V1 at 1050 K is 5965 kg m^{-3} [25], the heat capacity, C_p, is 771 J kg^{-1} K^{-1} and the thermal expansion coefficient is $\alpha_{liq} = 5.32 \times 10^{-5}$ K^{-1}. With $\kappa \cong 10$ W m K^{-1} and a viscosity of $\eta = 1.5$ Pa s at the diffusion temperature, Eq. (43) implies that the temperature differences, ΔT, inside the liquid should be smaller than 175 K. For comparison, within a system having a viscosity of 10^{-3} Pa s, typical for most metals, the temperature distribution has to be uniform within ca. 0.1 K in order to suppress convective flow.

With a modification of the present setup for the capillary flow experiments, a Au foil was inserted vertically into the liquid V1 [36]. After 400 s the sample with the Au foil was cooled to room temperature. The resulting spatial Au concentration, c_{Au}, was analyzed using a *Jeol JXA-733* microprobe and is shown in Fig 22. The maximum Au concentration within the liquid was less than 1.5 at-% in this experiment. An error function profile,

$$c_{Au}(x) = c_0 \operatorname{erfc}\left(\frac{x}{2\sqrt{D_{Au} t}}\right), \tag{44}$$

with

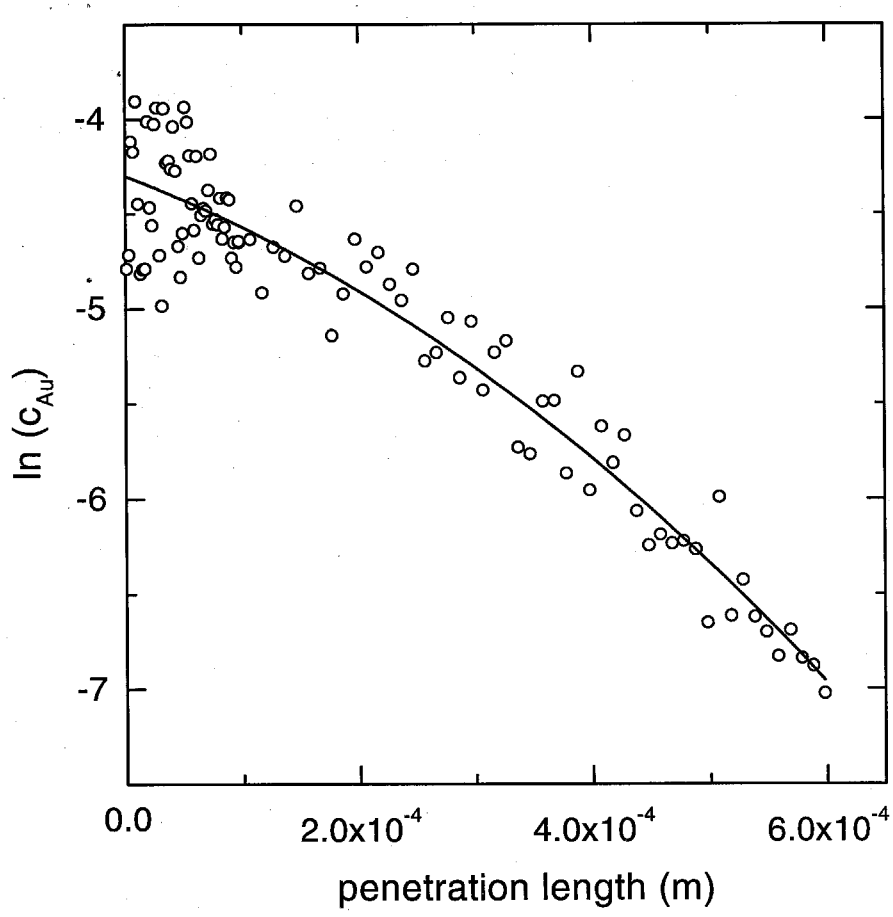

Fig. 22 Concentration profile of Au in V1

Atomic fraction, c_{AU}, of Au in V1 after diffusion at 1050 K and 400 s as measured by electron microprobe (○). The solid line (—) represents a complementary error function fit to the data, Eq. (44).

$$\mathrm{erfc}(z) = 1 - \frac{2}{\sqrt{\pi}} \int_0^z \exp\left(-u^2\right) du \tag{45}$$

was used to obtain the diffusion coefficient, $D_{Au} = 6.1 \times 10^{-11}\ \mathrm{m\,s^{-2}}$. The corresponding fit is also plotted in Fig 22.

Quasielastic neutron scattering experiments on V4 revealed that above the liquidus temperature the differences in the diffusion coefficients of the various elements in the liquid alloy are less than one order of magnitude [37]. This finding is in accordance with the merging tracer diffusion coefficients in Fig 22 and is well known for foreign diffusion in the equilibrium melts of Ag, Hg, Sn, Pb, and Bi [38].

4.2. Time Scales for Viscous Flow and Atomic Transport

In the following, time scales for viscous flow are compared to typical diffusion times in the liquid and supercooled liquid state of V1. From the temperature dependence of the viscosity data presented in chapter 3 and from published tracer diffusion data, the notion of solid-like and liquid-like atomic transport in the supercooled liquid will be discussed.

At temperatures below 650 K, the isothermal relaxation of the viscosity of V1 to its equilibrium values has been measured [16]. Similar to the viscosity relaxation in V4 [39], the internal equilibration times, τ_η, associated with this relaxation into the supercooled liquid state are found to be proportional to the viscosity:

$$\tau_\eta = \frac{\eta}{G_\eta}. \tag{46}$$

The experimental values of τ_η and η yield $G_\eta = 5.5 \times 10^8\,\mathrm{Pa}$ where the temperature

dependence of G_η is neglected compared to η and τ_η. Also, for simplicity, the following discussion will be based on a single equilibration time constant, τ_η, at each temperature, thereby neglecting non-exponential relaxation behavior. A more detailed analysis would include a spectrum of relaxation times [40].For long annealing and observation times, $t \gg \tau_\eta$, the system is said to be in the supercooled liquid state, while for short times, $t \ll \tau_\eta$, the sample reveals properties of a solid-like amorphous state.

The viscosity data from Fig 17 including the Cohen-Grest fit have been converted via Eq. (46) into equilibration times and the times are plotted in the form of an Arrhenius plot in Fig 23. The times τ_η in Fig. 23 are in good agreement with the total times for the calorimetric glass transition upon linear heating with rate R. From differential scanning calorimetry the latter are defined by $(T_g^{end} - T_g^{onset}) / R$ [29].

Note that τ_η is proportional but not equal to the relaxation time as defined within Maxwell's model of viscoelasticity [41, 42]. From the shear modulus of V1 of $G = 3.3 \times 10^{10}$ Pa [43] one expects the Maxwell time (η / G) for shear stress relaxation after *small* deformations to be about 2 orders of magnitude faster than the internal equilibration time τ_η.

Recently, studies of Be interdiffusion and Ni, Co, and Al radiotracer diffusion in deeply supercooled V1 were performed. Al diffusion in V1 should be only slightly faster than Zr due to the similarity of their atomic radii. Tracer diffusion studies of Al and Zr in V4 support this assumption [44]. Regardless of the exact diffusion mechanism of the various elements, a time τ_D may be defined for the successful

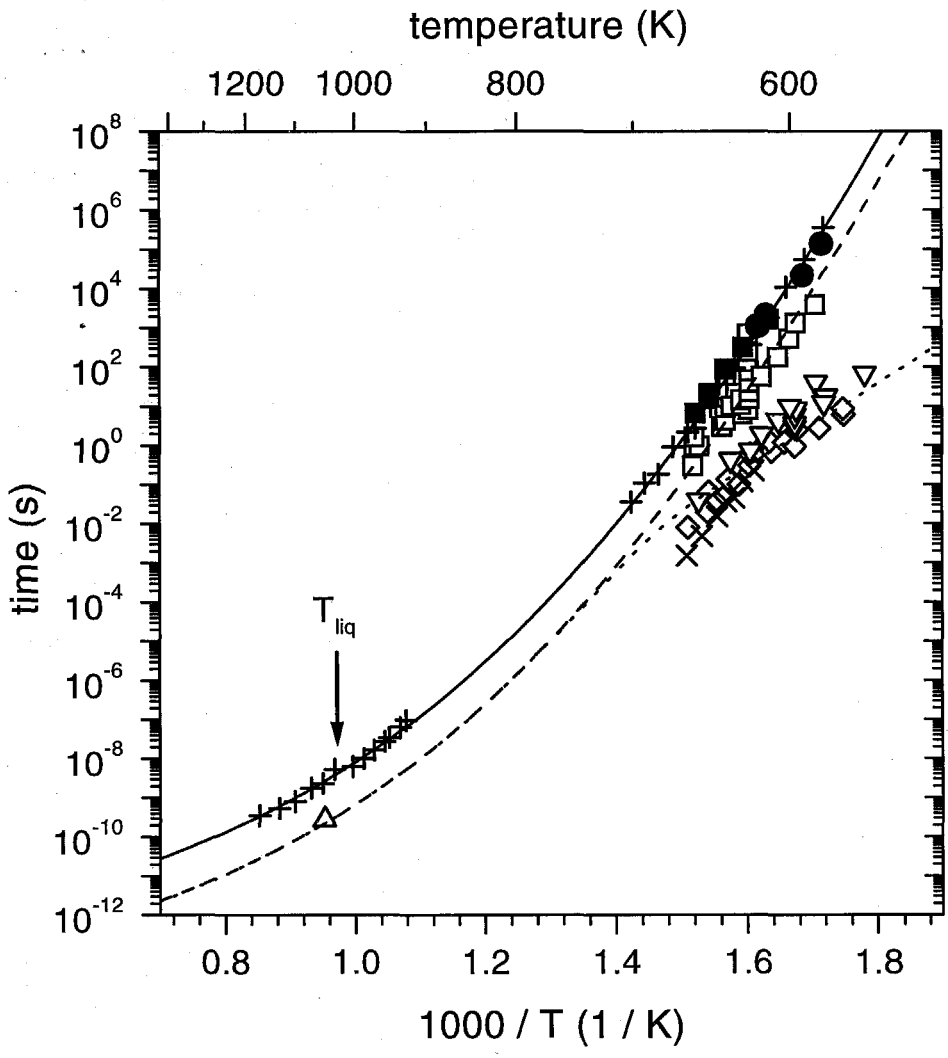

Fig. 23 Time scales in the liquid and supercooled liquid of V1

Thermal equilibration times, τ_η, (+) according to Eq. (46) and the Cohen-Grest fit (—) as well as times for the glass transition (•) [29] and relaxation times (▪) to reach the equilibrium viscosity [16]. Diffusion times from interdiffusion of Be (×) and Au (△) and tracer diffusion of Ni (◇), Co (▽), and Al (□), (---), see Eq. (47) and Eq. (48).

displacement of a tracer atom by a distance $l \equiv \sqrt{\overline{l^2}}$. For the i-th tracer, the Einstein equation for random walk reads:

$$\tau_{D,i} = \frac{l^2}{6 D_i}. \tag{47}$$

The times, $\tau_{D,i}$, correspond to the mean displacement of an average atomic diameter, l. Note that this definition of $\tau_{D,i}$ does not necessarily imply a jump mechanism. From the atomic volume, v_m, l is estimated to be 3.2×10^{-10} m and the corresponding $\tau_{D,i}$ are added in Fig 23. Around 600 K the diffusivities of Al and Ni differ by about 3 orders of magnitude, while they show a tendency to merge at higher temperatures. The Al diffusion shows temperature dependence similar to the internal relaxation time:

$$\tau_{D,Al} \cong 7.14 \times 10^{-2}\, \tau_\eta. \tag{48}$$

The proportionality factor implies that the mean displacement of an Al (Zr) atom in the supercooled liquid during a typical relaxation time is $\left(7.14 \times 10^{-2}\right)^{-\frac{1}{2}} l$ or roughly 4 interatomic diameters.

Ni and Co show significantly smaller absolute values of τ_D and activation energies of about 2.0 eV to 2.2 eV. Clearly, the time scales for viscous flow and diffusion of medium-sized atoms have different temperature dependencies in the deeply supercooled liquid state of V1. A collective hopping mechanism is likely to control the diffusion of Ni and Co in this temperature range as this could be confirmed for Co in V4 by isotope effect measurements [45]. Similarly, one expects the migration of the smallest atom in the alloy, Be, to be controlled by thermally activated jumps on a potential energy surface that fluctuates on a time scale given by τ_η.

Guided by the differences among the diffusion coefficients for various elements at low temperatures on the one hand and the scaling between viscosity and diffusion in the equilibrium liquid, a hybrid equation for the diffusion times, τ_D, of medium sized atoms in V1 is considered. Within this model, the time for a successful displacement, *l*, of, e.g., Ni can either be limited by viscous flow or by a solid-like jump, where Eq. (4) takes into account that both processes may occur parallel:

$$\frac{1}{\tau_{D,Ni}} = \frac{g_{Ni}}{\tau_\eta} + \frac{1}{\tau_{Ni,0}} \exp\left(-\frac{Q_{Ni}}{kT}\right). \tag{49}$$

At high temperatures $\tau_{D,Ni}$ is limited by the first term in Eq. (4), i.e., by the time scale for changes in the surrounding matrix, τ_η. The value of $g_{Al} = 14$ (see above) may serve as a lower limit and a first estimate for g_{Ni} as one does not expect Ni diffusion to be faster than Au near the liquidus (see Fig 22). The corresponding times, $\tau_{D,Ni}$, are plotted in Fig 23 with $Q_{Ni} = 2.1\,eV$. At sufficiently low temperatures, below about 800 K, thermally activated jumps of Ni with an average activation energy Q_{Ni} can occur as the potential energy barriers for Ni diffusion become fixed for the time between two successive jumps,. Both processes in Eq. (49) act in parallel in a relatively wide intermediate temperature range between about 700 K to 800 K, which can be regarded as the glass transition regime for Ni diffusion. This temperature range for the change in the atomic transport mechanism is independent of the time scale of the experiment but differs among the various components in the alloy. In fact, for the fast diffusing species (Ni, Cu, Be) in the alloy one expects a cascade of transitions. The jumps of a medium sized atom like Ni in the dense packed supercooled liquid will

probably also affect the positions of the fastest diffusor, Be. Description of the Be diffusion is therefore particularly difficult as its motion is affected by the collective movement of all other elements in the cascade of transitions.

5. CRYSTALLIZATION OF THE SUPERCOOLED LIQUID

The ability to form metallic glass by cooling from an equilibrium liquid is equivalent to suppressing crystallization within (certain regions of) the supercooled liquid state of the system. Consequently, experimental crystallization studies are a powerful tool for understanding the glass forming ability of metallic systems.

Monatomic or binary metals may be supercooled - in some cases up to several 100 K - below their melting points by containerless processing or fluxing techniques but critical cooling rates to form a glass are typically on the order of 10^7 to 10^9 K s^{-1}. To characterize the stability with respect to crystallization of a conventional monatomic or binary metallic systems in its supercooled liquid state, oftentimes only the minimum crystallization temperature, T_x, upon linear undercooling below the liquidus temperature is cited [46, 47].

Recently, crystallization studies [48, 49, 50] in the deeply supercooled liquid of multicomponent BMG forming alloys have found considerable attention. The experiments are made possible by the alloys' increased stability with respect to crystallization.

Most of the experiments have been performed by heating amorphous samples with a rate on the order of 1 K/s through the glass transition region into the supercooled liquid state [48, 51, 52]. This method is denoted by 'path A' in Fig 24. Commercially available calorimeters are well suited for these studies and results are found to be independent of the crucible material used. Only few data are available for thermophysical properties in the equilibrium or slightly supercooled liquid of BMG

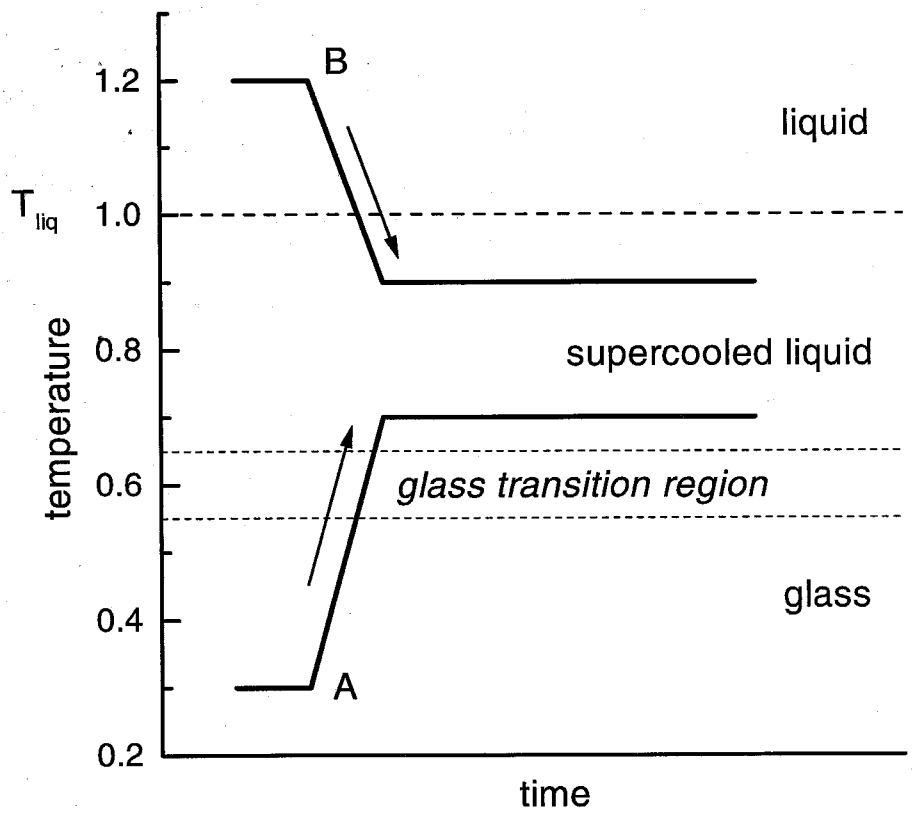

Fig. 24 Isothermal crystallization studies of the supercooled liquid state

Path A: Heating of amorphous samples, prepared, e.g., by melt quenching through the glass transition region. Path B: supercooling of the liquid below the liquidus temperature.

forming alloys. The high affinity of the transition metal alloys for impurities like oxygen poses severe challenges for experimental studies at high temperatures. However, the temperature range between the liquidus temperature, T_{liq}, and the temperature with the minimum time to crystallization, T_n, is decisive for the glass forming ability of the system [53, 54] as will be discussed below.

In this work, isothermal anneals of the supercooled liquid along path B in Fig 24 are performed in which the equilibrium liquid serves as the 'as-prepared' state compared to the amorphous solid in path A. Experiments in the supercooled liquid are oftentimes performed under non-isothermal conditions, i.e., either cooling from the equilibrium liquid or heating from the amorphous solid state. Subsequent isothermal anneals of the supercooled liquid, schematically shown in Fig 24, are possible only for relatively good glass formers, that allow for an experimental time window of at least some 10 seconds before the onset of crystallization. The good glass forming ability of V1, represented by a critical cooling rate of 1 K/s [55], allows for these isothermal experiments.

The critical cooling rate for glass formation, as used in the present work, is defined as the minimum rate at which an equilibrium liquid has to be cooled to keep the crystalline volume fraction to a small but finite value, e.g., 10^{-3}. In this sense, an amorphous solid may contain a small amount of crystals. Whether a finite volume of an amorphous sample is completely crystalline-free or whether it contains a small volume fraction of crystals depends on the details of the crystallization process, e.g., the nucleation and growth rates. In most metals the presence of a single crystalline nucleus may trigger the crystallization of the entire sample because of the large growth

velocities of the crystals in the supercooled metallic liquid. In good glass formers like commercial soda-lime-silica glasses, on the other hand, unwanted crystalline impurities have a marginal effect on the glass forming ability because the growth velocity of the crystalline phase(s) is small. The growth velocity will play a central role in the interpretation of the experimental results presented in this chapter.

Of particular concern in the study of supercooled liquids is the liquidus temperature of the alloy defining the boundary between the equilibrium and the supercooled liquid. While in principal well defined within the Zr-Ti-Cu-Ni-Be phase diagram, this transition is difficult to detect experimentally. Differential thermoanalysis (DTA) scans with heating rates of 20 K/min on as-quenched V1 are shown in Fig 25. For this experiment, a *Setaram DSC 2000* was equipped with graphite crucibles machined from *POCO DFP-1* graphite. The He (99.9999%) purge gas was purified using a heated titanium getter type *Matheson 8301* and the instrument was calibrated using the melting points of pure Al (99.9999%) and Ag (99.99%).

The first run (solid line in Fig 25) depicts the glass transition region from ca. 625 K to 655 K and at least four exothermic events from 716 K to 810 K. In the past, much attention has been given to the onset of crystallization from the amorphous state of V1 in the temperature range from ca. 600 K to 750 K [29, 48, 51, 56]. At these (low) temperatures, metal or ceramic containers may be used to anneal the material in conventional furnaces. In contrast, experimental studies in the vicinity of the liquidus temperature require either levitation techniques or the use of compatible crucible materials. A series of endothermic peaks from 935 K to 1035 K in Fig 25 indicates the melting of crystalline phases.

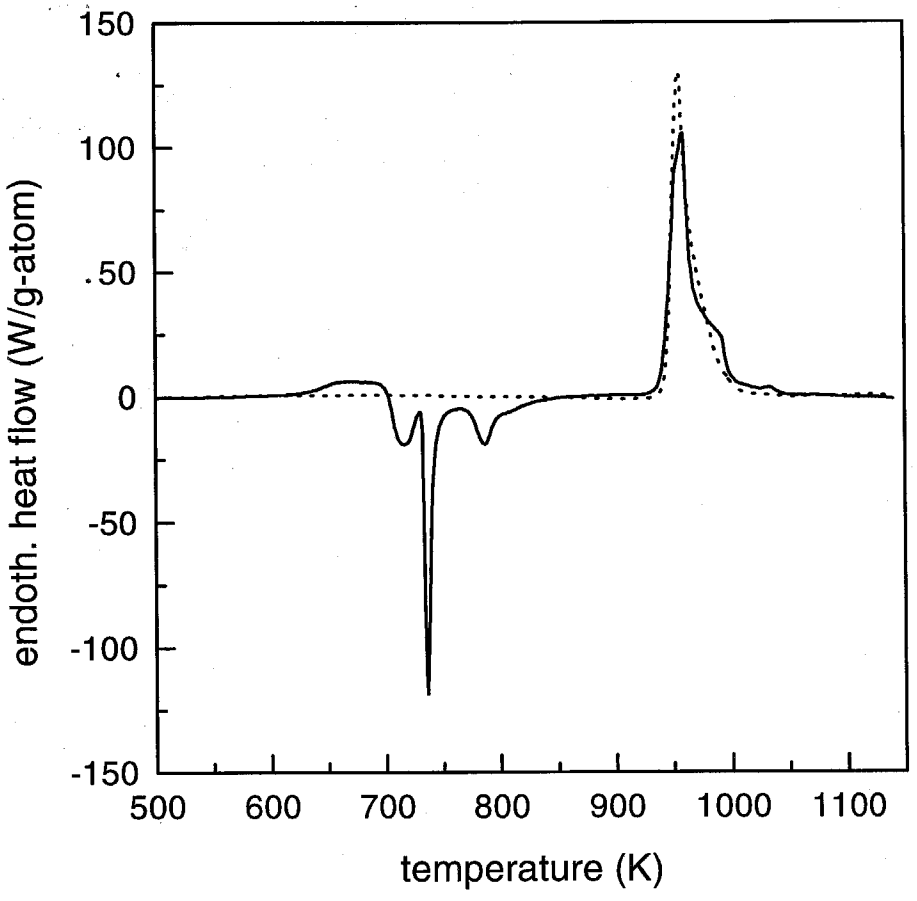

Fig. 25 Differential thermoanalysis upon linear heating

Heating of as-quenched, amorphous V1 (——) and slowly (0.1 K/s) cooled, crystallized V1 (- - -) in a Setaram DSC 2000 differential thermal analyzer with heating rates of 0.33 K/s. Both scans have been corrected by the baseline obtained from empty crucibles.

Subsequently, the sample is slowly cooled to room temperature (ca. 0.1 K/s) and then the second DTA scan (dotted curve) is recorded upon reheating. The absence of the glass transition and the exothermic crystallization events shows that the sample completely crystallized upon cooling from the liquid state after the first run. The endothermic melting signal in the second DTA trace has a different shape compared to the first run. In particular, it is somewhat sharper and the highest peak (1035 K) can no longer be resolved. The slow cooling after the first run apparently resulted in a different crystalline microstructure compared to the crystals that formed upon heating from the amorphous state. As only the relative heights of peaks up to 1026 K shift, the liquidus temperature was taken to be $T_{liq} = 1026\,K$. The good stability of the DTA baselines for T > 1050 K, obtained by using high purity graphite instead of alumina crucibles, leads to a slightly higher liquidus temperature than previously reported [29].

Cooling from the equilibrium liquid of V1 to room temperature with rates as low as 0.9 K/s to 1.2 K/s is sufficient to form metallic glass [57]. In Fig 26 time-temperature profiles with a slightly higher cooling rate of about 2 K/s are shown. For these experiments, the shear cell in the apparatus that was described in chapter 2.1 was exchanged with graphite crucibles of 4 mm diameter, containing ca. 140 mg of V1. After annealing the samples in vacuum (10^{-1} Pa) at the indicated temperatures for 360 s, the RF power supply was switched off and the cooling by radiation and conduction via the crucible mount is monitored. The recalescence upon crystallization can be best seen in the derivative of the time-temperature signal, shown for two cooling curves in the inset of Fig 26. The endothermic heat signal reduces the cooling rate by about 0.2 K/s for ca. 30 s. The shape of the peak in the cooling rate curve

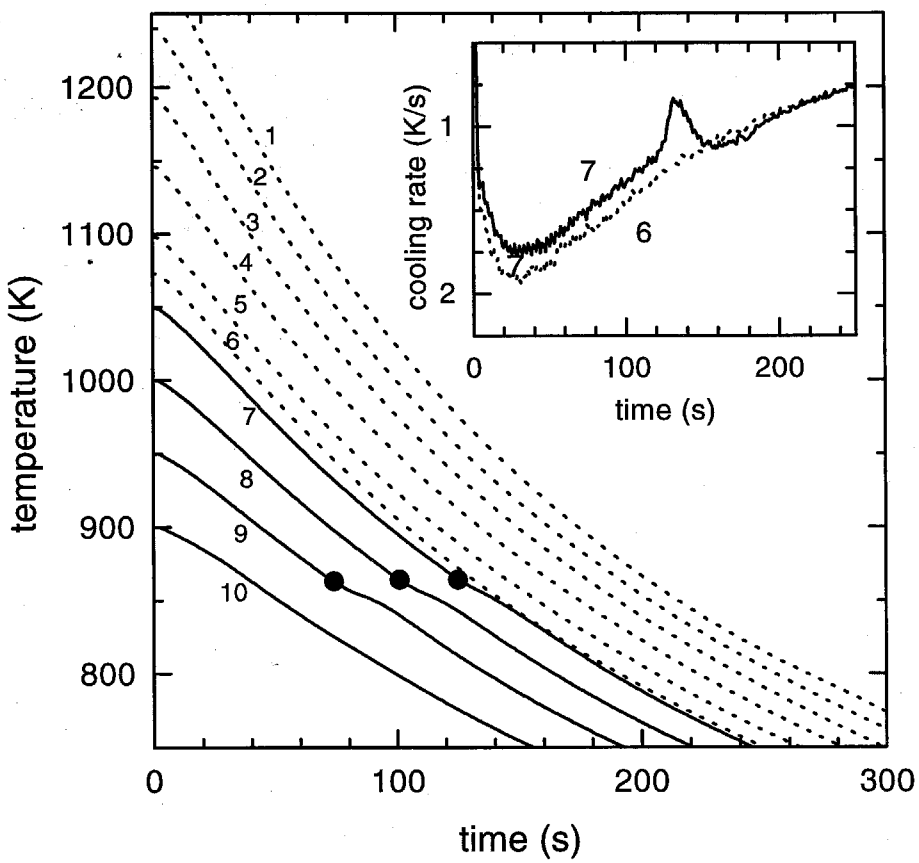

Fig. 26 Cooling curves from the equilibrium liquid state

Cooling of V1 contained in graphite crucibles from various temperatures. Recalescence events (•) observed in the temperature-time profiles are indicated. The inset shows the (negative) derivatives of the temperature with respect to time, i.e., the cooling rate. The curves 1-10 correspond to starting temperatures of 1300 K, 1250 K, 1200 K, 1150 K, 1100 K, 1075 K, 1050 K, 1000 K, 950 K, and 900 K. Experiments 1-6 (···) resulted in amorphous and 7-10 (—) in crystalline material.

depends on the size and geometry of the crucible used and the amount of V1 used. In addition, the wetting of the (liquid) sample on the graphite is crucial for a precise time and therefore temperature measurement of the onset of crystalliztion upon cooling. As this wetting is not achieved with, e.g., Zn, Al, Ag, or Au, a reproducible calibration of the peak area to the amount of the heat released by the sample was not possible.

In Fig 26 crystallization is not observed upon cooling from initial temperatures exceeding 1050 K. This temperature is only slightly higher than the liquidus temperature measured upon heating in the DTA. To form metallic glass by cooling from the liquid, the sample has been superheated above its liquidus temperature by only 30 K.

While the increased stability of V1 compared to simple metallic systems makes a detailed experimental analysis of the temperature and rate dependence of crystallization from the supercooled liquid possible, characterization of the primary crystalline phase and the thermodynamic driving force is complicated in this multicomponent system. The basic crystallographic structure of the primary phases that form in the Zr-Ti-Cu-Ni-Be system is known [58], but a detailed thermophysical analysis is not yet available. From, e.g., heat capacity measurements, so far only the specific Gibbs free energy difference, ΔG, between the liquid and a crystalline phase mixture is known (see Fig 27). The interpretation of ΔG as the driving force for the crystallization is valid only in the case of a polymorphic transformation. Similarly, one usually has to use a crystalline phase mixture of V1 as a reference state for specific volume measurements [25].

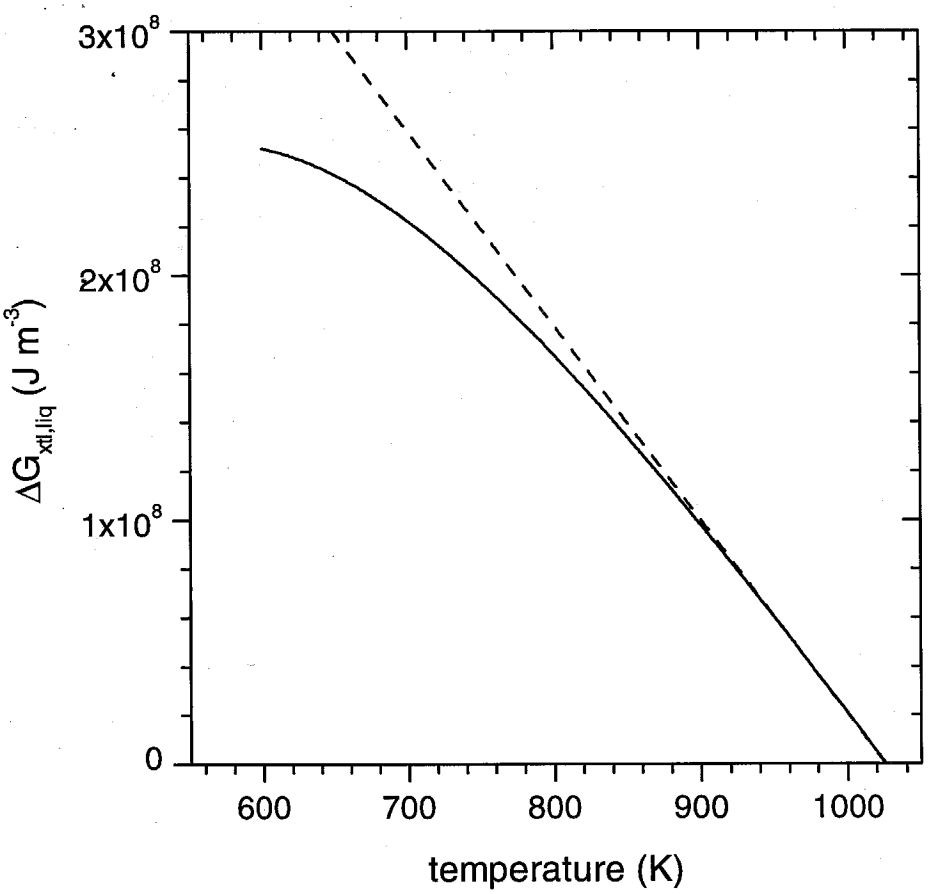

Fig. 27 Driving force for crystallization

Specific Gibbs free energy difference between the supercooled liquid and the crystalline state (—) as obtained by integrating Eq. (50) with the experimental results for the specific heat capacity difference, Δc_p, given by Eq. (30) and Eq. (31). Linear approximation (---), Eq. (51), used in the classical nucleation and growth model.

The specific Gibbs free energy difference, ΔG, between the liquid and the crystalline phase results from differential scanning calorimetry (DSC) [29], yielding a lower limit for the driving force for primary crystallization. In calculating ΔG from the measured specific heat capacities (Eq. 30 and Eq. 31) via

$$\Delta G = \Delta H_f - \Delta S_f T_{liq} - \int_T^{T_{liq}} \Delta c_p(\tilde{T})\, d\tilde{T} + T\int_T^{T_{liq}} \frac{\Delta c_p(\tilde{T})}{\tilde{T}}\, d\tilde{T}\,, \tag{50}$$

it will be sufficient to use a linear approximation for the temperature dependence,

$$\Delta G \cong 7.992 \frac{(T_{liq} - T)}{K} \frac{J}{K\,g\text{-}atom}, \tag{51}$$

for the following phenomenological discussion of chapters 5.1 and 5.2.

5.1. Crystallization: Isothermal

With the computer controlled induction furnace designed for the viscosity measurements described in chapter 2, it is also possible to study the temperature dependence of the onset of crystallization in the supercooled liquid state of V1. For this purpose 4 mm diameter graphite crucibles containing ca. 0.05 cm^3 of V1 replace the concentric cylinder shear cell. The small crucibles allow for cooling rates of up to 40 $K\,s^{-1}$ to be applied to the liquid prior to the isothermal anneals. The recalescence upon crystallization can be observed in the thermocouple signal. An example of a measured time-temperature profile is shown in Fig 28 (a). The onset of crystallization is best observed in the time derivative of the temperature reading, i.e., in the heating rate curve shown in Fig 28 (b).

The logarithm of the onset times, t_x, of the first recalescence event versus the inverse annealing temperature are summarized in Fig 29. As the comparison to results

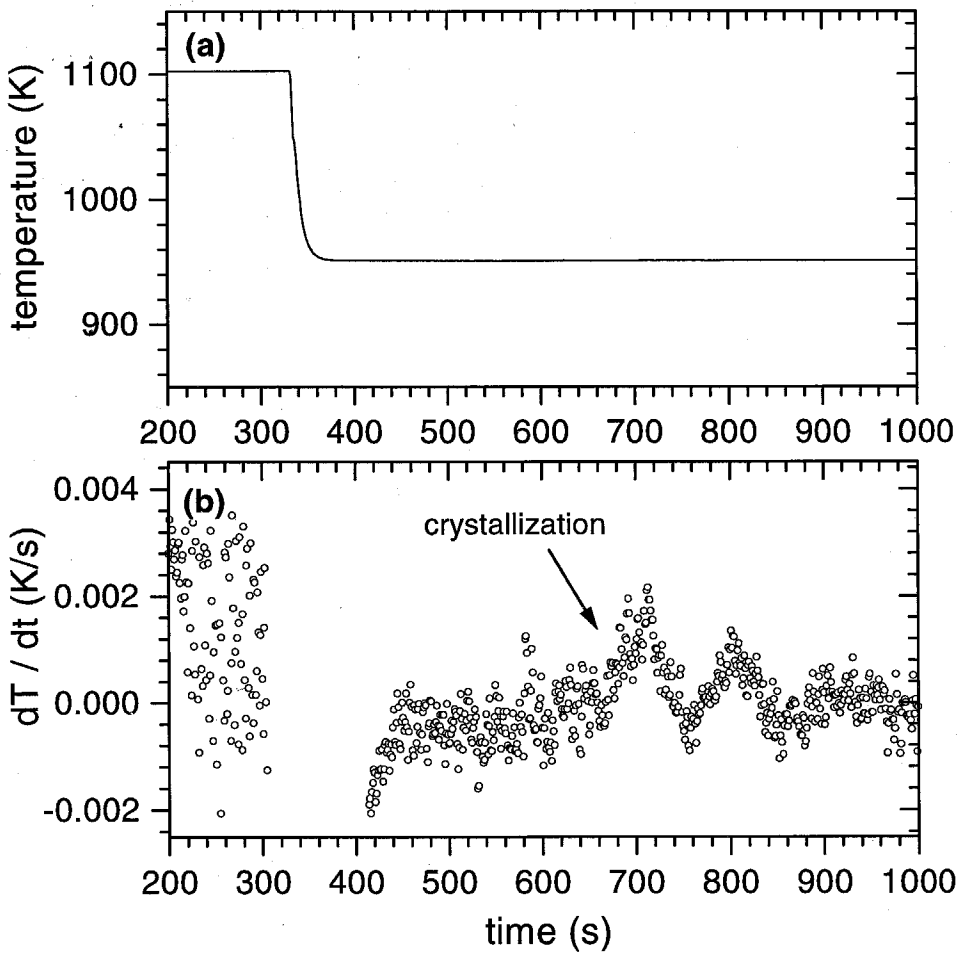

Fig. 28 Time-temperature profile for isothermal anneals of supercooled V1

(a) Temperature, T, of a 4 mm diameter graphite crucible containing 86 mg V1 as a function of the annealing time, t. (b) Derivative, dT/dt, showing the temperature rise due to the heat release upon crystallization.

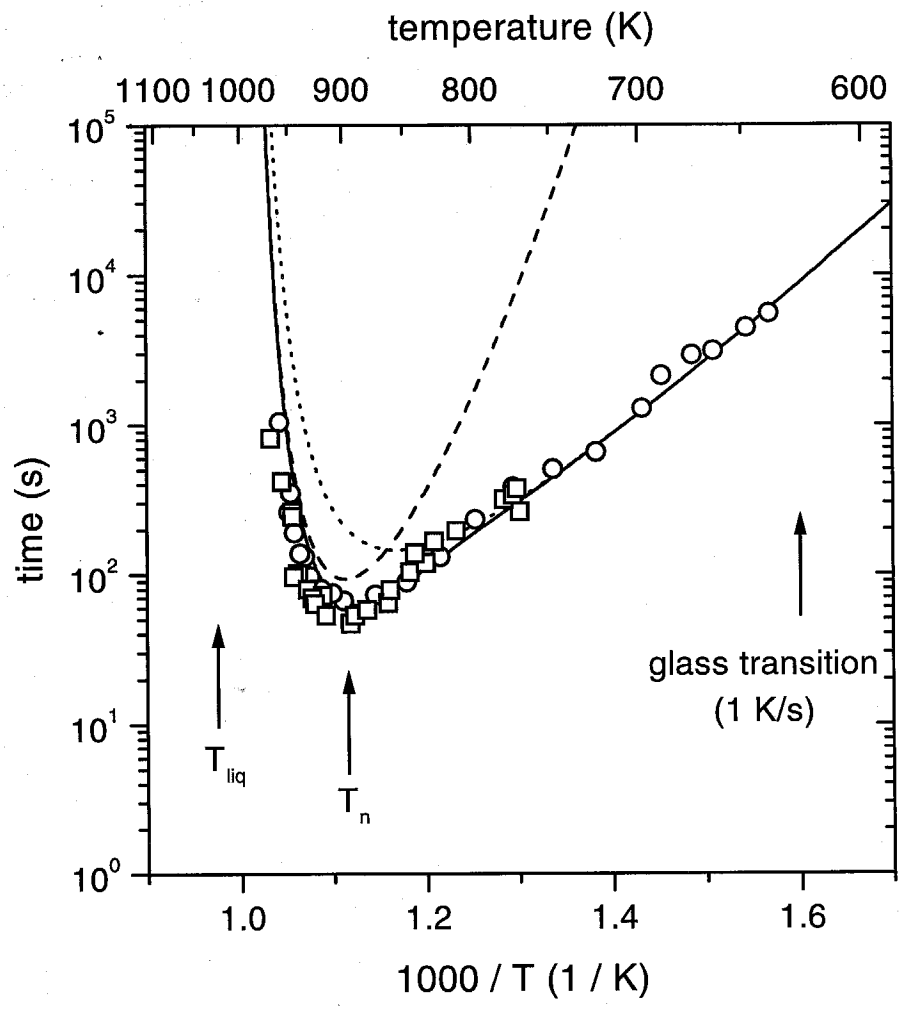

Fig. 29 Time-temperature-transformation (TTT) diagram

Primary crystallization from the supercooled liquid state of V1 contained in graphite crucibles (○) and processed by ESL (□). Least-squares fits of Eq. (58) with $x = 0.001$ (—). The contribution from the viscous (---) and from the Arrhenius term (···) in Eq. (58) are indicated.

from electrostatic levitation experiments [55] shows, the graphite containers do not appreciably alter the crystallization behavior in comparison to containerless processing [59]. In spite of the presence of the crystalline crucible walls, the transformation kinetics of the supercooled liquid are unchanged within the resolution of the experiment. Obviously, the crystallization of the bulk sample is not triggered by surface crystallization at the container interface.

The experimental data in Fig 29 show a minimum at $T_n = 895$ K. This behavior is well known for a large variety of materials [2] and arises from the competition between increasing thermodynamic driving force for crystallization and decreasing atomic mobility upon supercooling. The shortest times to crystallization are as large as 60 s at this temperature, reflecting a critical cooling rate for glass formation of only 1 K/s. This rate is at least 6 orders of magnitude larger than values estimated for simple metallic systems. At the temperature T_n the viscosity of V1 is about 4 orders of magnitude larger than the viscosity of, e.g., Ni at a similar degree of supercooling (see Fig 10). Apparently, the sluggish kinetics at elevated temperatures discussed above acccount for a significant part of V1's exceptional glass forming ability.

Classical nucleation theory is often used to quantify the time and temperature dependence of crystallization from a supercooled liquid [50]. In its simplest form, the steady-state nucleation rate,

$$I_s = A\, D_{eff} \exp\left(-\frac{\Delta G^*}{kT}\right), \tag{52}$$

is written as a product of an effective diffusivity, D_{eff}, and a thermodynamic Boltzmann factor to overcome a nucleation barrier for crystal formation. For

homogeneous nucleation of spherical particles [2], the latter includes the Gibbs free energy,

$$\Delta G^* = \frac{16\pi\sigma^3}{3\Delta G^2}, \tag{53}$$

to form a critical nucleus. The exact form of the specific Gibbs free energy difference, $\Delta G(T)$, between the liquid and the crystal and the values for σ in Eq. (53) are of particular importance for the shape of the TTT diagram at the high temperature end, $T > T_n$. The bottleneck for nucleation at low temperatures, $T < T_n$, is the kinetic factor, D_{eff}, in Eq. (52).

The interfacial energy, σ, is treated as a fit parameter in Eq. (53). A temperature dependent interfacial energy can be included [60], but for simplicity it is omitted in the following discussion.

The growth velocity, u, of the crystalline phase can, to a first approximation, be expressed as a product of a kinetic and a thermodynamic factor:

$$u = \frac{f D_{eff}}{l}\left[1 - \exp\left(-\frac{v_m \Delta G}{kT}\right)\right]. \tag{54}$$

An effective diffusivity, D_{eff}, as above is used and the fraction of sites at the liquid-crystal interface where atoms are preferentially added or removed is taken to be $f = 1$.

The crystallized volume fraction, x, will depend on both the nucleation rate and the growth velocity. In general, the nucleation rate and the growth velocity can be both time- and temperature-dependent. Considering three-dimensional growth and the steady-state nucleation rate from Eq. (52), the time-dependent 'extended' volume

fraction, x_e, of crystallized material is obtained by integrating over all nucleation events:

$$x_e(t) = \frac{4\pi}{3} \int_0^t I(T,\tau) \left[\int_\tau^t u(T,t')\, dt' \right]^3 d\tau \,. \tag{55}$$

The double time integral sums over all nucleations events, occurring at time, τ, and takes into account the crystal growth from time, τ, to time, t. In the derivation of the quantity x_e in Eq. (55), it is assumed that all growth centers continue to grow unimpeded for all times, t, giving rise to the term 'extended' crystallized volume fraction, x_e. For isothermal anneals and steady state nucleation, Eq. (52) and Eq. (54) inserted in Eq. (55) yield with a simple integration [53]:

$$x_e = \frac{\pi}{3} I_s\, u^3\, t^4 . \tag{56}$$

Consequently, the time, t_x, to crystallize a small volume fraction, x, can be written as:

$$t_x = \left(\frac{3\, x_e}{\pi\, I_s\, u^3} \right)^{\frac{1}{4}} . \tag{57}$$

Except for the effective diffusivity, D_{eff}, one is left with A and σ as the only two fit parameters in Eq. (57).

In order to simulate the minimum in the nucleation time at 895 K in Fig 29 with Eq. (57) and the commonly used relation, $D_{eff} \sim \eta^{-1}$, the parameter $\sigma = 0.040$ Jm^{-2} has to be chosen. The relatively high temperature of the 'nose' in the TTT diagram implies a rather small interfacial energy compared to values of 0.06 Jm^{-2} to 0.3 Jm^{-2} reported for monatomic liquid metals [46]. The smaller the interfacial energy, σ, the smaller the nucleation barrier in Eq. (53). This suggests that the good glass forming

ability of V1 is not based on the interfacial properties between the supercooled liquid and the nucleating crystals.

In Fig 29, for temperature T < 800 K, the logarithm of the onset of crystallization is approximately proportional to the inverse temperature: $\log(t_x) \sim 1/T$. In this temperature range, the thermodynamic driving force, ΔG, has virtually no influence on the slope of the $\log(t_x)$ versus $1/T$ plot, because the kinetic factor, D_{eff}, dominates in Eq. (52) and Eq. (54). Therefore, Eq. (57) yields $t_x \sim D_{eff}^{-1}$, which implies an Arrhenius-like effective diffusivity: $D_{eff} \sim \exp(-Q_{eff}/kT)$ for the low temperature part of the TTT diagram.

The effective activation energy, Q_{eff}, in Fig 29 is on the order of 1 eV, substantially smaller than the apparent activation energies for viscous flow of more than 3 eV shown in Fig 21. All viscosity and crystallization data were obtained on samples in their supercooled liquid state and the failure of the viscosity to describe the onset times of crystallization can therefore not be connected with the calorimetric glass transition [61].

The temperature dependence of the tracer diffusion coefficients of medium-sized atoms was discussed in chapter 4.2. A hybrid equation, Eq. (49), for the diffusivity was proposed that combined the contributions from viscous flow at high temperature with thermally activated hopping at low temperatures within the supercooled liquid. It is tempting to use an expression similar to Eq. (49) for the effective diffusivity, D_{eff}. However, the effective diffusivities and activation energies used to describe kinetics at liquid-solid interfaces during crystallization in a multicomponent system are not

equivalent to (bulk) tracer diffusion coefficients. The collective transport mechanisms that were proposed to control atomic transport in the bulk of the Zr-based glass forming alloys [45] are likely to be somewhat altered near a crystalline cluster.

From Eq. (56) one finds $x_e \sim D_{eff}^4$ and with the proposed hybrid equation, the temperature and time dependence of x_e takes the form:

$$x_e(T,t) = P_1 T\left[\frac{1}{\eta(T)} + P_2 \exp\left(-\frac{Q_{eff}}{kT}\right)\right]^4 \ldots$$

$$\ldots\left[1-\exp\left(-\frac{v_m \Delta G}{kT}\right)\right]^4 \exp\left(-\frac{16\pi\sigma^3}{3\Delta G^2}\right) t^4 . \qquad (58)$$

As in Eq. (49), the kinetic term (first line) in Eq. (58) is an additive superposition of a viscous and an Arrhenius term. For simplicity, a VFT relation may be used in Eq. (58) for the temperature dependence of the viscosity instead of the Cohen-Grest formula.

In Fig 29 the crystallization times were fitted with the aid of Eq. (58) solved for the time, t (solid curve). The contributions from the viscous term (dashed curve) and the Arrhenius term (dotted curve) in Eq. (58) are indicated in Fig 29. The large apparent activation energies for viscous flow at low temperatures overestimate the temperature dependence of the crystallization times. The assumption that $D_{eff} \sim \eta^{-1}$ is therefore not valid in the vicinity of the glass transition temperature.

The fit of the hybrid equation, Eq. (58), to the data in Fig 29 yields the nucleation rate, $I(T)$, and the crystal growth velocity, $u(T)$. Both curves are shown in Fig 30. Again the contributions from the viscous and the Arrhenius term are indicated. One notes that the maximum of the nucleation rate is located close to the temperature, T_n,

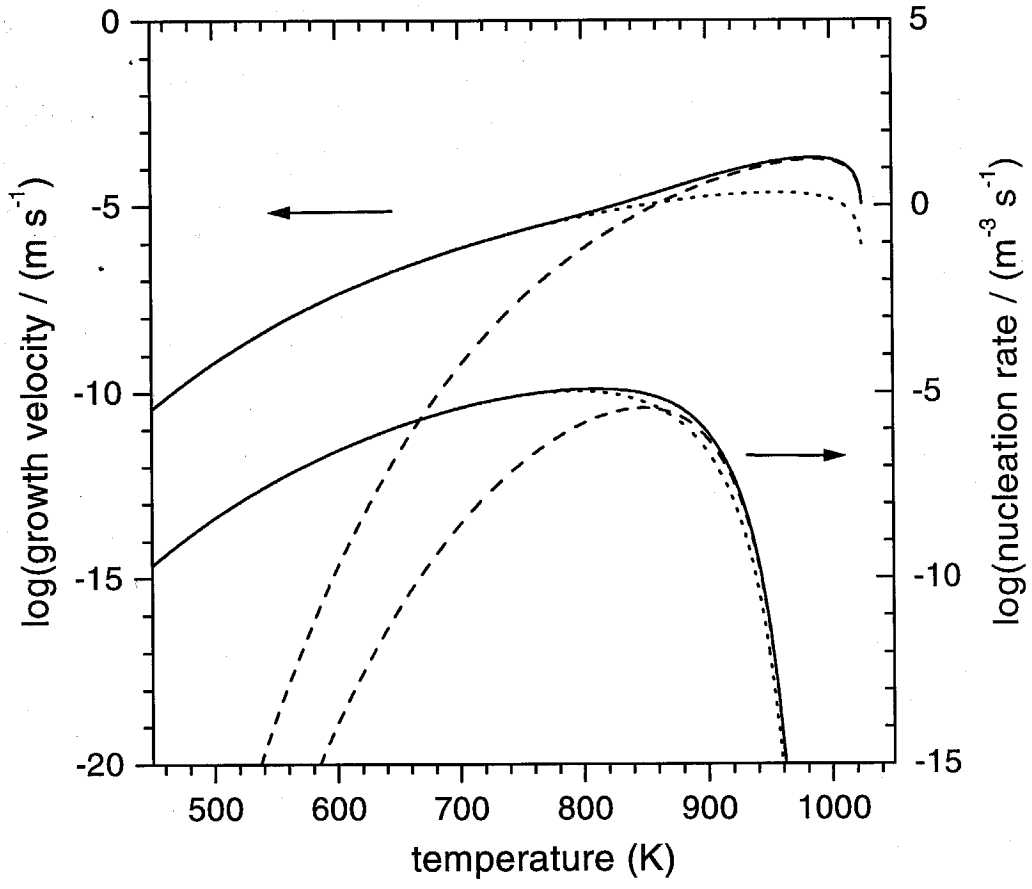

Fig. 30 Nucleation rates and growth velocities in supercooled V1

Left axis: Growth velocity, u, calculated according to Eq. (54) with a maximum at 985 K. Right axis: nucleation rate as calculated according to Eq. (52).

with the minimum time to crystallization. In contrast, the growth velocity has its maximum at a significantly higher temperature of 985 K. The growth velocity will play a central role in the discussion of the critical cooling and heating rates to bypass crystallization, presented in the following chapter.

It was assumed in the derivation of Eq. (57) and Eq. (58) that the volume fraction, x_e, is much smaller than unity, i.e., that Eq. (57) is only applicable to the early stages of crystallization. With increasing volume fraction of the crystalline phase, individual crystals will impinge each other and the rate of crystalline growth will decrease as x approaches unity. Frequently, the later stages of crystallization are analyzed according to the formalism proposed by Johnson, Mehl, Avrami, and Kolmogorov (JMAK) [62]. The transformed volume fraction, x, is written as

$$x = 1 - \exp\left[-x_e(t)\right], \tag{59}$$

where x_e is given by Eq. (56) in the case of isothermal anneals or, more generally, by Eq. (55). The crystallized volume fraction, x, according to the JMAK formalism of Eq. (59), is plotted in Fig 31 (a) as a function of temperature and the logarithm of the time elapsed. Although the results in Fig 31 are based on the assumption of a continuous transformation from the liquid to the crystalline state ($x_e \sim t^4$), most of the volume of the supercooled liquid crystallizes in a fairly narrow time interval for a given temperature.

The rate, *dx/dt*, of the volume fraction crystallized per unit time, plotted in Fig 31 (b), is approximately equal to the heat release observed in an isothermal calorimetric crystallization experiment. One notes that at each temperature, $T < T_{liq}$, a well defined crystallization peak arises after an apparent incubation time, even under

(a)

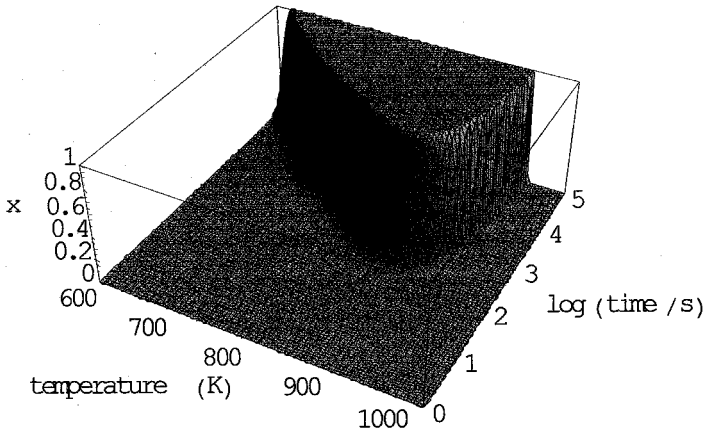

(b)

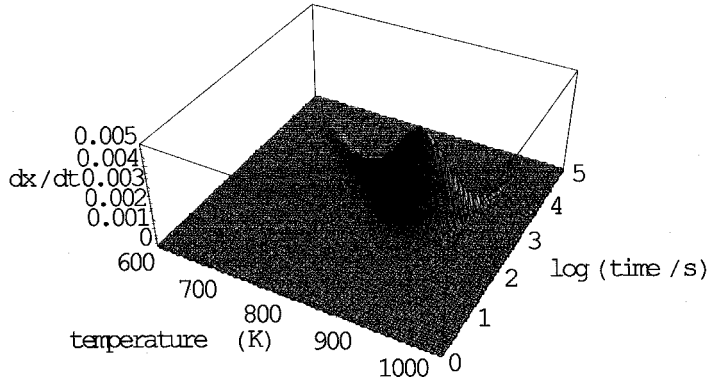

Fig. 31 Crystallized volume fraction and rate of transformation

(a) Crystallized volume fraction, x, of V1 according to Eq. (59) versus temperature and the logarithm of the time elapsed. (b) Crystallization rate, dx/dt, as a function of the temperature and the logarithm of the time.

the assumption of steady state nucleation and growth under isothermal conditions, i.e., $x_e \sim t^4$ in Eq. (58). The height of the crystallization peak, dx/dt, in Fig 31 shows a maximum in the vicinity of the temperature T_n. The latent heat of crystallization is released in a minimum amount of time near T_n. Thermoanalysis studies at significantly lower or higher temperatures than T_n result in crystallization peaks that are more spread out in time and therefore smaller in magnitude (see, e.g., Fig 28).

On the basis of the present experimental data. it is yet unclear to what extent the assumption of a steady state nucleation rate has to be modified for the present system. Results from microstructure analysis indicate that the nucleation rate used above serves as a lower limit and that transient nucleation events are partly responsible for the long nucleation times, i.e., for the good glass forming ability of the alloy [58].

5.2. Crystallization: Linear Cooling and Heating

One of the central quantities in theoretical and experimental studies on glass formation is the critical cooling rate, $R_{c,cr}$, to bypass crystallization upon cooling from the equilibrium liquid [2]. It is commonly used to quantify the glass forming ability of a liquid.

The practical importance of the critical cooling rate stems from the fact that it is linked to the maximum thickness, d_{max}, of a quenched amorphous ingot. The size of the smallest dimension of the ingot is limited by the requirement that heat must be conducted from the center of the sample to its surface. In the case of perfect heat extraction from the surface, d_{max} is (up to a factor of order unity) given by [63]

$$d_{max} \cong \sqrt{\frac{1}{R_{c,cr}} \frac{\kappa_{liq} M_{mol} T_{liq}}{c_{p,liq} \rho_{liq}}}. \quad (60)$$

In Eq. (60), κ_{liq} is the thermal conductivity (W m^{-1} K^{-1}), ρ_{liq} the density (kg m^{-3}), and $c_{p,liq}$ the specific heat capacity (W g-atom^{-1} K^{-1}) of the liquid. M_{mol} is the alloys molar mass (kg g-atom^{-1}). With typical values for the Zr-based metallic glass forming systems of $\kappa_{liq} \cong 10\ \mathrm{W\,m^{-1}\,K^{-1}}$, $M_{mol} \cong 0.06\ \mathrm{kg\,g\text{-}atom^{-1}}$, $T_{liq} \cong 1000\ \mathrm{K}$, $c_{p,liq} \cong 40\ \mathrm{J\,g\text{-}atom^{-1}\,K^{-1}}$, and $\rho_{liq} \cong 6000\ \mathrm{kg\,m^{-3}}$, Eq. (60) yields:

$$\frac{d_{max}}{\mathrm{m}} \cong 0.05 \left(\frac{R_c}{\mathrm{K\,s^{-1}}} \right)^{-\frac{1}{2}}. \quad (61)$$

With a critical cooling rate of ca. 1 K/s this results in a maximum thickness of ca. 50 mm for V1 and with R_c = 9 K/s of ca. 18 mm for V4. These dimensions agree well with the maximum size ingots prepared by quenching the liquid in copper molds.

In Fig 32 the experimentally observed critical cooling rate and the onset temperatures of crystallization for smaller cooling rates are shown in the form of a semi-logarithmic time-temperature plot. As for the isothermal crystallization studies, the liquid metal was contained in graphite crucibles heated inside the computer-controlled induction furnace described in chapter 2.

The continuous-cooling-transformation (CCT) diagram, Fig 32, shows that the decisive temperature range for glass formation is between ca. 850 K and the liquidus temperature. Once the liquid is successfully supercooled below ca. 850 K with a constant cooling rate, the crystallization kinetics have practically become slow enough for the sample to reach the amorphous state.

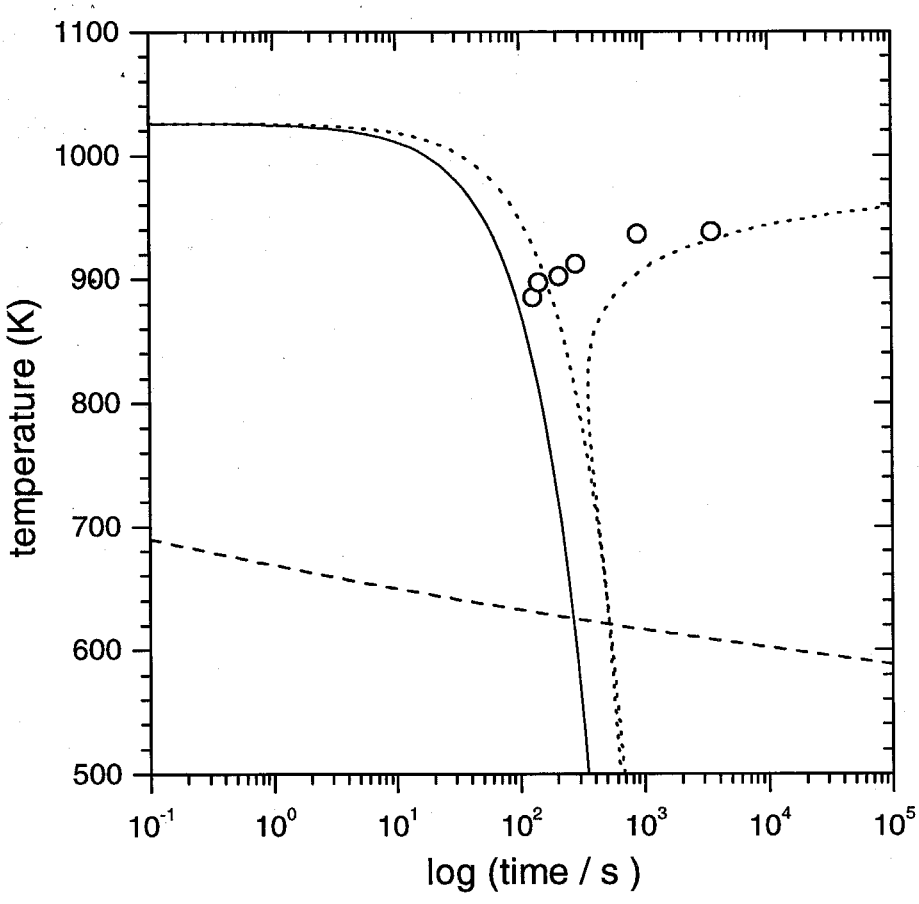

Fig. 32 Continuous-cooling-transformation (CCT) diagram

Linear cooling experiments from the equilibrium liquid of V1. Experimentally observed onsets of crystallization (○) with varying cooling rate. Time temperature profile for the critical cooling rate is indicated (—). Continuous cooling transformation (CCT) diagram as calculated from Eq. (55) for x = 0.001 (···). The average structural equilibration times marking the glass transition region are also indicated (---).

The crystallized volume fraction during linear cooling with cooling rate, α, can be calculated with the aid of Eq. (55). For this purpose the time-temperature profile,

$$T(t) = T_{liq} - \alpha t, \tag{62}$$

is inserted into Eq. (55) together with the nucleation rate, I_s, and the growth velocity, u, from Fig 30. The integrals in Eq. (55) can be solved numerically, lowering the temperature from the liquidus temperature in steps of 1 K/s of duration 1 K/α. For each temperature step the crystallized volume fraction, x, is calculated according to Eq. (55).

The times, t_x, where the numerical solution of the integrals yields $x = 0.001$ have been calculated for various cooling rates, α, and are indicated in Fig 32 (dotted curve). The agreement between this calculated CCT diagram and the experimental data in Fig 32 is satisfactory - the critical cooling rate, e.g., predicted by the calculations is only a factor of two larger than the experimentally observed rate.

With the present setup, it is possible to study the crystallization behavior of the supercooled liquid upon heating with rates up to 200 K/s. An example for heating an 8 mm diameter graphite crucible in conjunction with a 5-turn, 42 diameter RF coil at 70% power setting of the *LEPEL* RF power supply is shown in Fig 33 (a). To achieve the highest accuracy in the temperature reading a *Labview VI* without a PID control algorithm was used and the thermocouple voltages were written to the hard drive only after the experiment had finished. With this configuration, it is possible to sample the thermocouple voltage with a sampling rate of 6000 Hz. Upon completion of the temperature scan, digital data smoothing was performed by averaging 100 adjacent temperature readings, yielding an effective scan rate of 60 Hz.

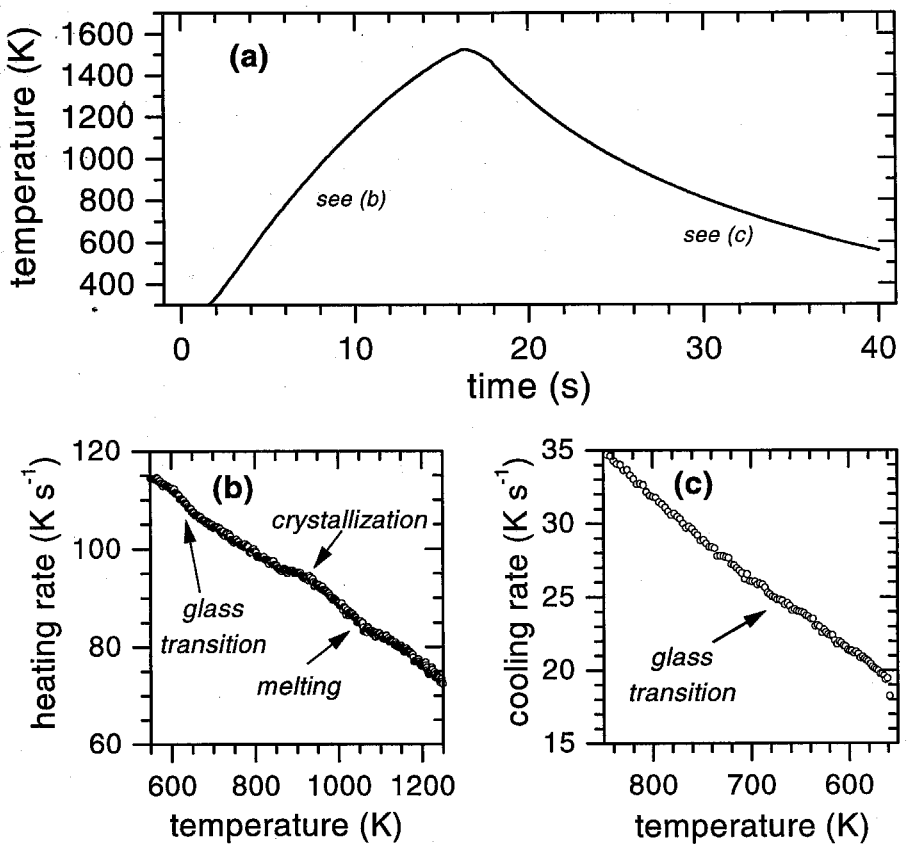

Fig. 33 Time-temperature profile of a fast heating and cooling experiment

Time-temperature profile (a) as measured by a thermocouple inserted in the graphite crucible wall. Heating rate (b) and cooling rate (c) as obtained by differentiation showing the glass transition, crystallization and melting of the sample.

The differentiated time-temperature curve upon heating, Fig 33 (b), shows the glass transition, crystallization, and melting upon heating. At the indicated heating rate of ca. 60 K/s, the temperature difference, ΔT_x, between the midpoint of the glass transition and the onset of crystallization is as large as 205 K. This is roughly double the temperature range achieved with conventional heating rates on the order of 0.1 K/s.

In Fig 34 heating rate curves with rates up to ca. 300 K/s for both amorphous and crystallized samples are shown. At the highest heating rate, the onset of crystallization of the supercooled liquid and subsequent melting is no longer detectable. For comparison, the heating rate curves of crystallized V1 samples are also shown in Fig 34. Here, the melting of the crystalline phases can clearly be identified in the differentiated temperature signal for all heating rates. The times and temperatures of the onset of crystallization are summarized in Fig 35 together with previously published data from crystallization studies using a *Perkin Elmer DSC 7* [29]. The supercooled liquid is slightly more stable against crystallization when processed in the high purity graphite crucibles. At heating rates on the order of 0.1 K/s, the temperature interval, ΔT_x, is larger by ca. 30 K compared to the published results [29]. The question whether this effect is due to the incorporation of a small amount of carbon into the alloy [64] or a consequence of the higher purity of the processing environment in the present setup is the subject of further investigations [65].

The stability of the supercooled liquid upon heating above the glass transition region is oftentimes characterized by the size of the temperature interval,

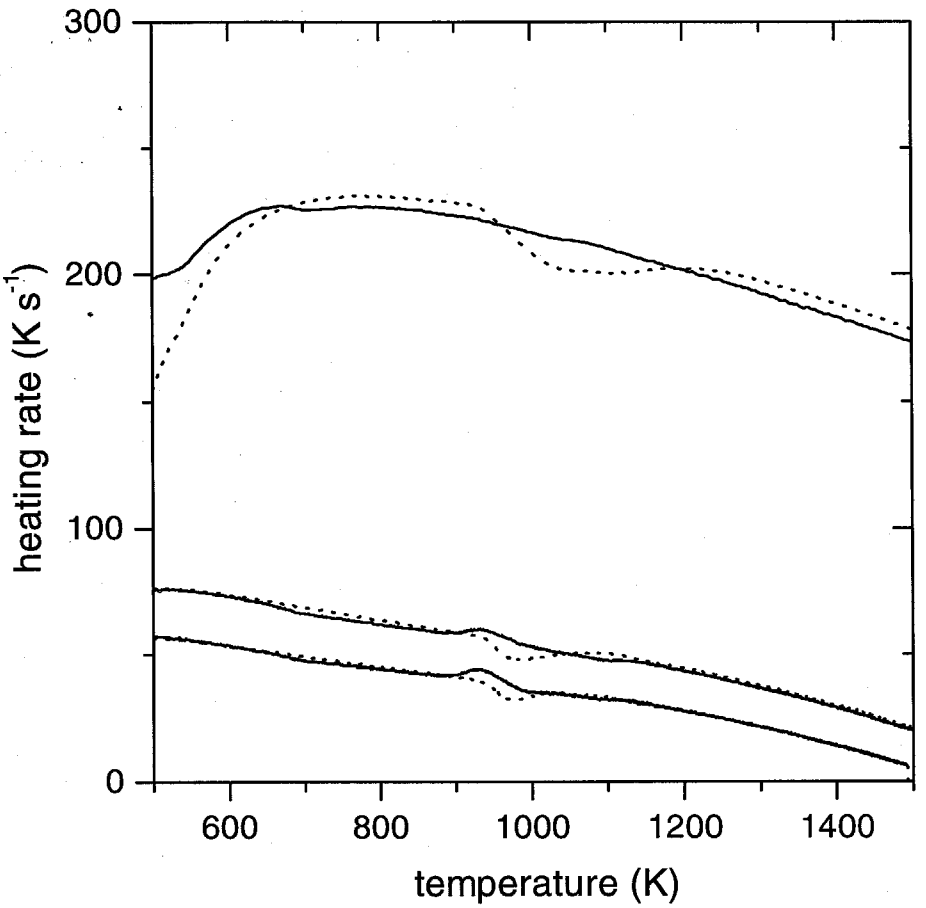

Fig. 34 Thermoanalysis of V1 upon fast heating

Heating rates, dT/dt, as determined from measured time-temperature profiles. The solid curves (—) represent experiments starting with amorphous V1 and the dotted curves (···) are heating rate curves starting with completely crystallized samples.

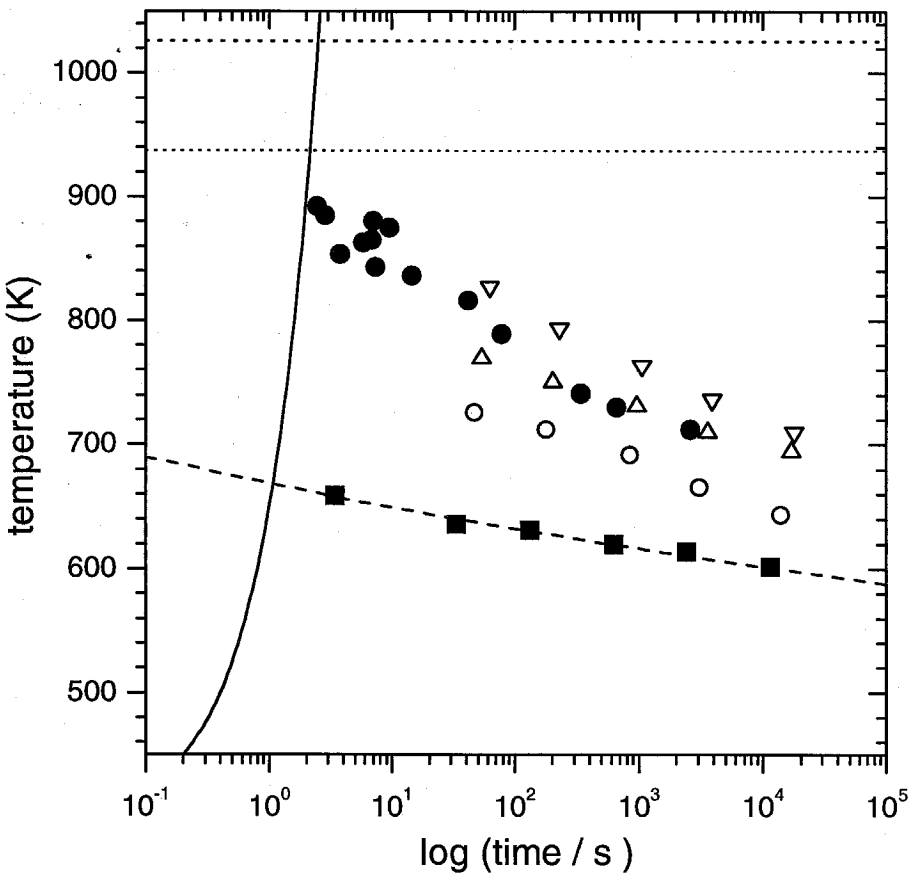

Fig. 35 Continuous-heating-transformation (CHT) diagram

Onset of crystallization (•) as measured with the present setup and published results (○,△,▽) for the three main exothermic events in DSC scans as well as the time-temperature profile (—) for the critical heating rate of 200 K/s. Average times for the glass transition region are also plotted (■).

$$\Delta T_x(R_h) = T_x(R_h) - T_g(R_h), \tag{63}$$

between the onset of the glass transition and onset of the first crystallization event. The notion of the temperatures, T_g, T_x, and ΔT_x in Eq. (63), is only meaningful in conjunction with a heating rate, R_h.

Usually, the temperature range that is decisive for the glass forming ability of the material is not accessible by heating amorphous metallic samples through the glass transition region. The width of the supercooled liquid region upon heating, ΔT_x, is therefore only a crude and indirect measure of the glass forming ability of the system.

The present experimental results for the onset times of crystallization in Fig 32 and Fig 35 show a difference between the critical cooling and the critical heating rate of about two orders of magnitude. The time dependence of the crystallized volume fraction according to Eq. (55) can qualitatively explain this difference between the critical cooling and the critical heating rate as described in the following.

Starting with $x = 0$ at $T = T_{liq}$, the extended crystallized volume fraction for successive temperature steps of one Kelvin of duration 1 K/α are computed via Eq. (55). The volume fraction, x, is easily computed via Eq. (59) and the results are plotted in Fig 36 (curve a). Upon cooling from the liquidus temperature, x increases continuously and becomes approximately constant at 600 K. Note the logarithmic scale of the volume fraction from 10^{-9} to 1. The simulation is terminated at 450 K. This 'freezing' of the crystallization kinetics can be attributed to the strong decrease in D_{eff} in Eq. (52) and Eq. (54), hindering further nucleation and growth of crystals. The total crystallized volume fraction of 0.035% for the simulated cooling curve in Fig 36 will not be observed in the thermocouple signal of the experimental setup used. Also,

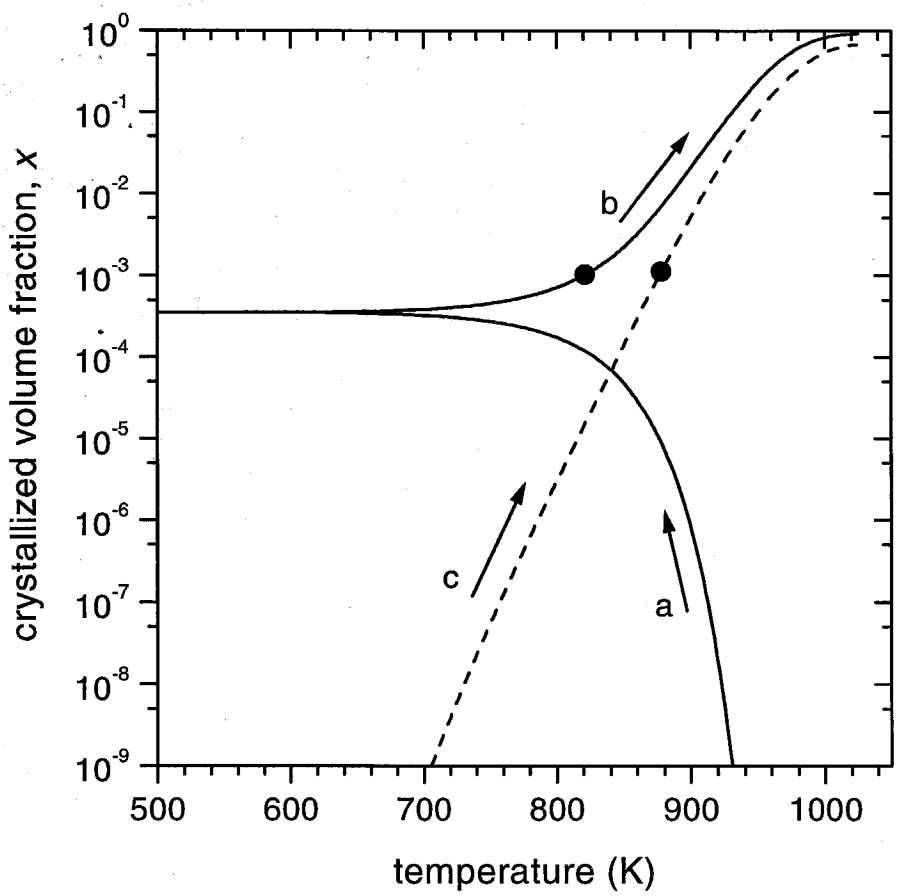

Fig. 36 Crystallized volume fraction for continuous cooling and heating

Cooling from the equilibrium melt with 1 K/s (a) resulting in a volume fraction of crystalline material of 3.52×10^{-4} *and re-heating with 1 K/s (b). For comparison, heating from a crystalline-free solid with 1 K/s (c). All curves are calculated with the aid of Eq. (55) and Eq. (59).*

such a small amount of crystals will go undetected in a conventional x-ray diffraction experiment.

The simulation is continued, now starting at 450 K with the crystal distribution obtained during cooling. As can be seen in Fig 36 (curve b), the crystallized volume fraction increases during heating as new nuclei are formed and the existing crystals continue to grow. The temperature of 820 K at which $x = 0.001$ is indicated.

For comparison, a simulation starting with a perfectly amorphous sample, $x = 0$, at 450 K is also shown in Fig 36 (curve c). The sample reaches $x = 0.001$ at 880 K. In this simulation, during heating from the purely amorphous state, the exact same number of nuclei form as during cooling. This stems from the assumption of steady-state nucleation. However, the nuclei formed are exposed to different growth upon cooling and heating, respectively.

As shown in Fig 30, the growth rate calculated according to Eq. (54) has a maximum at a relatively high temperature of 985 K within the supercooled liquid range. Upon heating, nuclei forming at, e.g., the minimum in TTT diagram at T_n, will be exposed to these high growth rates before reaching the liquidus temperature. In contrast, the nuclei that form upon cooling at T_n will experience less favorable growth rates. Starting with a crystal-free amorphous solid, the volume fraction crystallized upon heating to the liquidus temperature with a constant rate will be higher than the volume fraction crystallized upon cooling with the same (negative) rate.

Mathematically, this difference results from the difference in integrating over the growth rate, u, in Eq. (55) for heating and cooling respectively. In Fig 36 the sample cooled with 1 K/s from T_{liq} to 450 K contains 0.035% crystals, while the one heated

from 450 K to T_{liq} is 92% crystallized. If the effect of quenched-in crystals is taken into account (see Fig 36), the difference is even more severe. The critical cooling rate required to keep the average crystallized volume fraction to a certain (small) value is therefore smaller than the corresponding critical heating rate. For the present system, the calculations yield $R_{c,cooling}$ = 1 K/s and $R_{c,heating}$ = 9 K/s, which are shown in Fig 32 and Fig 35, respectively.

5.3. Crystallization at constant shear rate

Shear induced changes in the microstructure have been experimentally observed in a variety of polymers as well as silica-based liquids [66, 67, 68] and have been the subject of theoretical calculations [69, 70, 71]. Both shear-induced mixing as well as shear-induced decomposition has been observed for various systems. It has been suggested that in metallic systems the presence of a (high) shear rate should suppress the formation of crystals in the supercooled liquid.

With the setup described in chapter 2, a constant shear rate may be applied to the supercooled liquid while, simultaneously, heat releases during solidification are recorded from the thermocouple signal. The viscosity of V1 as measured with the concentric cylinder viscometer during linear cooling is shown in Fig 11. The onset of solidification can be seen in the deviation from Newtonian behavior.

The time-temperature profiles recorded during viscosity measurements shown in Fig 11 are plotted in Fig 37 (a). Initially, the cooling rate, shown in Fig 37 (b), is 0.66 K/s. With the deviation from Newtonian behavior, marked by open circles in Fig 37 (a), a small decrease in the cooling rate, i.e., a small exothermic event, can be

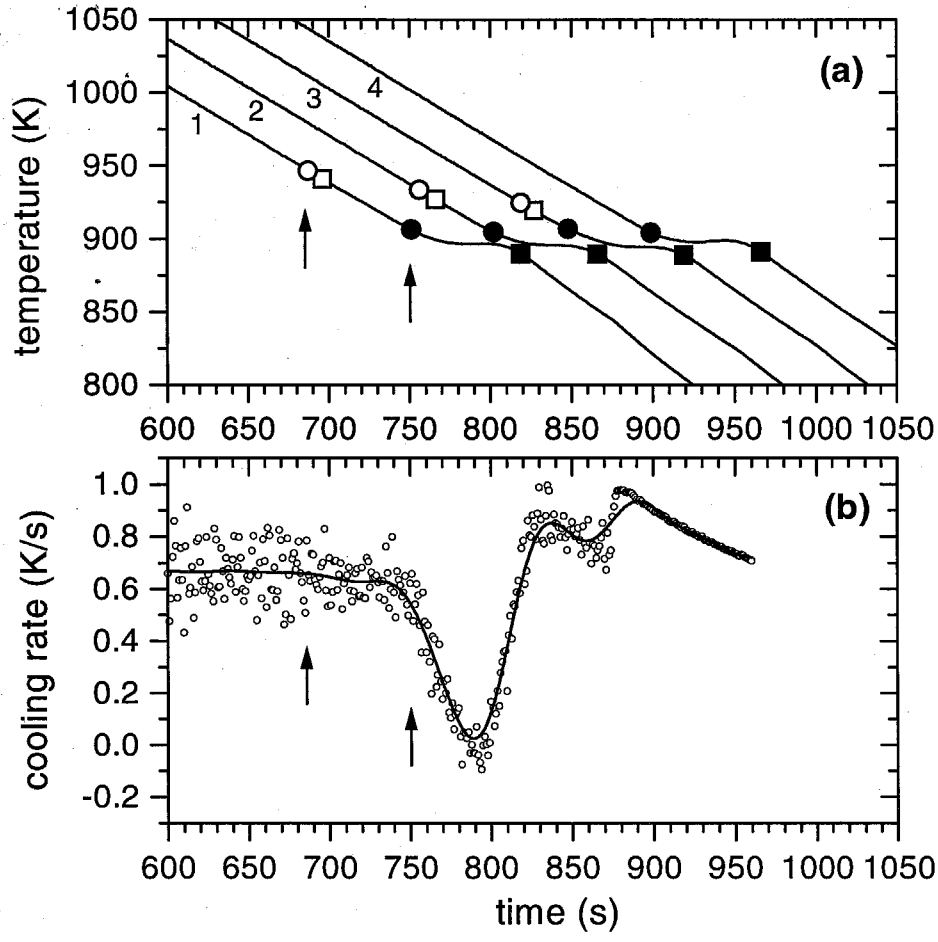

Fig. 37 Linear cooling curves at constant shear rate

Temperature (a) and cooling rate (b) during cooling from the equilibrium melt of V1 under constant shear rate. The curves 1-4 correspond to shear rates shown in Fig. 11. The onset of deviations from the equilibrium viscosity (○) and the onset (●) and endpoint (■) of the main crystallization peak are indicated. The rotation of the inner cylinder was stopped manually (□). The cooling rate data in (b) were smoothed (—) to guide the eye.

detected in Fig 37 (b). The sharp increase in viscosity in Fig 11 by over one order of magnitude occurs prior to the onset of the main recalescence, as shown in Fig 37.

A similar behavior of V1 was already observed at temperatures in the vicinity of the glass transition region [16]. It was suggested that the supercooled liquid phase separates into two liquids prior to the onset of crystallization. The strong increase in viscosity is likely to arise from the continuous phase having a higher viscosity than the initial supercooled liquid. Long relaxation times of the viscosity to its new equilibrium value after the phase separation support this view.

Whether the precursor to crystallization at high temperatures, shown in Fig 11 and Fig 37, is also connected with phase separation in the supercooled liquid is yet unknown. In experiments in the vicinity of the glass transition temperature, it is possible to quench the supercooled liquid during the onset of crystallization in to room temperature without significant changes in the microstructure during the quench. Subsequently, the microstructure can be investigated with standard techniques. In contrast, cooling the liquid from temperatures $T \gtrsim 850$ K during the onset of crystallization with cooling rates of less than 100 K/s resulted in completely crystallized material. The mechanism for primary crystallization at elevated temperatures is not yet understood in full detail.

The shear rate dependence of the onset of deviations from the equilibrium viscosity and the onset and endpoints of the main recalescence are summarized in Fig 38. A larger shear rate leads to deviations from Newtonian flow at higher temperatures. The position of the main crystallization peak remains unchanged within the resolution of the experiments. One should note that the stepping motor was

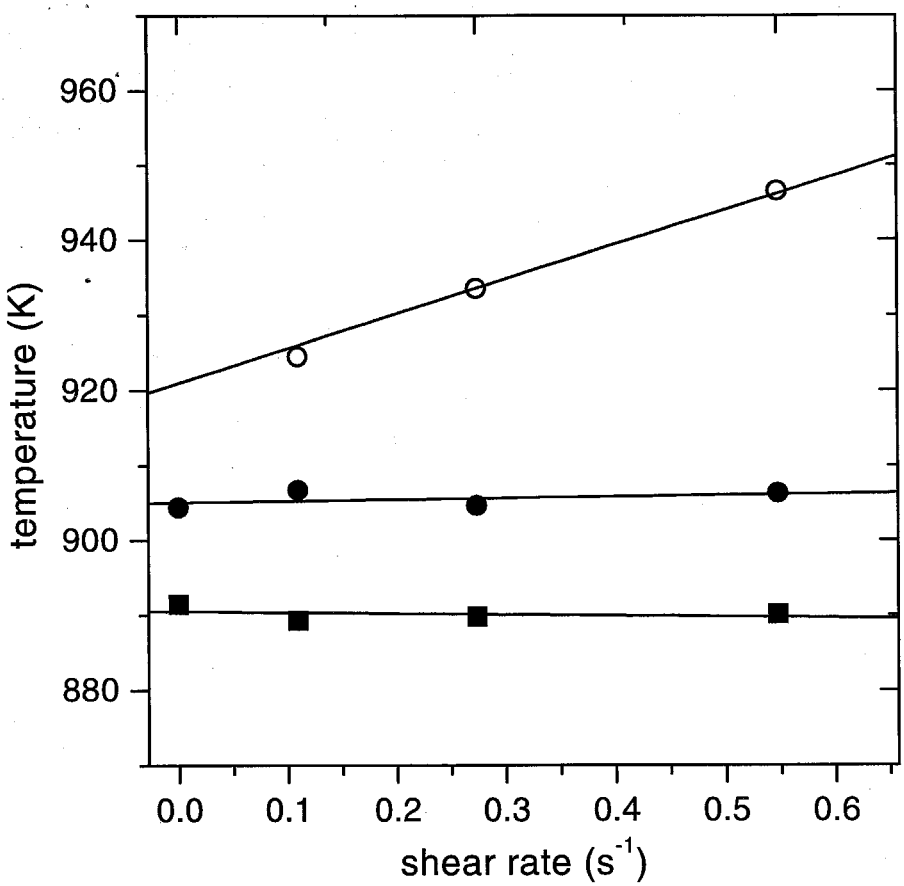

Fig. 38 Shear rate dependent solidification

Temperatures of onset of deviations from the equilibrium viscosity (○) as a function of the applied strain rate for a cooling rate of 0.66 K/s. Corresponding onset (●) and endpoint (■) temperatures of the main recalescence event are also indicated.

switched off, i.e., the shear flow was terminated (open squares in Fig 37 (a)), shortly after the increase in viscosity in Fig 11 to protect the shear cell from damage. The strain rates applied in the present experiments did not exceed 1 s^{-1} and are therefore much smaller than the strain rates proposed to influence crystallization in, e.g., melt-spinning.

6. SUMMARY

The viscosity of the V1 bulk metallic glass forming alloy was measured over a temperature range from 927 K to 1173 K in the equilibrium and supercooled liquid. The viscosity at the liquidus temperature of 2.3 Pa s is about three orders of magnitude larger than the viscosity of any pure metallic liquid. The free volume theory as formulated by Cohen and Grest describes the temperature dependence of the viscosity of V1 over 14 orders in magnitude.

The temperature dependence of the viscosity is found to scale with the time scales for diffusion of large atoms like Au or Al. The relaxation times obtained from the viscosity measurements suggest that in the deeply supercooled liquid the diffusion of small and medium sized atoms is governed by thermally activated jumps. A hybrid equation is proposed that takes into account the displacement of atoms through spontaneous fluctuations in the surrounding matrix as well as through thermally activated processes.

Liquid V1 could be successfully supercooled inside high purity graphite crucibles. The container walls are found to have no influence on the times to crystallization under isothermal conditions. The critical cooling rate of V1 contained in graphite is less than 2 K/s. The sluggish kinetics that are reflected in the high viscosity in the supercooled liquid state contribute significantly to the good glass forming ability of the alloy.

The onset of crystallization under isothermal conditions as well as upon heating from the amorphous state was studied in detail. The critical heating rate to bypass

crystallization was measured to be 200 K/s and the difference between the critical cooling and the critical heating rate can be qualitatively understood in the framework of nucleation and growth. Deviations from classical nucleation and growth theory found in rheological and crystallization studies at constant shear rate suggest that changes in the morphology of the supercooled liquid of V1 occur as a precursor of crystallization.

7. REFERENCES

[1] N.W. Ashcroft and N.D. Mermin, *Solid State Physics* (Saunders College, 1976)

[2] P.G. Debenedetti, *Metastable Liquids* (Princeton University Press 1996)

[3] C.A. Angell, Science, **267**, 1924 (1995)

[4] D. Turnbull, Contemp. Phys. **10**, 473 (1969)

[5] P. Duwez, Trans. ASM **60**, 607 (1967)

[6] W.N. Wham, American Laboratory, **30**, 1 (1998)

[7] J.L.M. Poiseuille, Comptes Rendus **11**, 961 (1840)

[8] F.M. White, *Viscous Fluid Flow* (Mc-Graw-Hill, New York, 1991)

[9] Omega Engineering, Inc., *The Temperature Handbook* (1995)

[10] P.K. Kundu, *Fluid Mechanics*, (Academic Press, 1990)

[11] M.M. Couette, Ann. Chim. Phys. **21**, 433 (1880)

[12] E.W. Washburn, Phys. Rev. **17**, 273 (1921)

[13] K.H. Tsang, S.K. Lee, and H.W. Kui, J. Appl. Phys. **70**, 4837 (1991)

[14] E. Bakke, R. Busch, and W.L. Johnson, Appl. Phys. Lett. **67**, 3260 (1995)

[15] G. Wilde, G.P. Görler, K. Jeropoulos, R. Willnecker, and H.J. Fecht, Mater. Sci. Forum **269-272**, 541 (1998)

[16] A. Waniuk, R. Busch, A. Masuhr, and W.L. Johnson, Acta mater. **46**, 5229 (1998)

[17] A. Inoue, Y. Kawamura, T. Shibata, and K. Sasamori, Mater. Trans, JIM, **37**, 1337 (1996)

[18] I. Egry, G. Lohöfer, I. Seyhan, S. Schneider, and B. Feuerbacher, Appl. Phys. Lett. **73**, 462 (1998)

[19] R. Busch and W.L. Johnson, Mater. Sci. Forum, **269-272**, 577 (1998)

[20] N.H. March, *Liquid Metals* (Cambridge University Press, 1990)

[21] G. Trapaga, R.W. Hyers, and M.C. Flemings, *International Workshop on Nucleation and Thermophysical Properties of Undercooled Melts* (Physikzentrum Bad Honnef, 1998)

[22] T. Iida and R.I.L. Guthrie, *The Physical Properties of Liquid Metals* (Clarendon, Oxford, 1988)

[23] W.L. Johnson, private communications

[24] S. Glasstone, K.J. Laidler, and H. Eyring, *The Theory of Rate Processes* (McGraw-Hill, New York, 1941)

[25] K. Ohsaka, S. K. Chung, W. K. Rhim, A. Peker, D. Scruggs, and W.L. Johnson, Appl. Phys. Lett. **70**, 726 (1997)

[26] C.A. Angell, Science, **267**, 1924 (1995)

[27] R. Busch, A. Masuhr, E. Bakke, and W.L. Johnson, Mater. Sci. Forum, **269-272**, 547 (1998)

[28] G. Adam and J.H. Gibbs, J. Chem. Phys. **43**, 139 (1965)

[29] R. Busch, Y.J. Kim, and W.L. Johnson, J. Appl. Phys. **77,** 4039 (1995)

[30] R. Busch, W. Liu, and W.L. Johnson, J. Appl. Phys. **83** (1998) 4134

[31] G.S. Grest and M.H. Cohen, Adv. Chem. Phys. **48,** 455 (1981)

[32] A. Masuhr, R. Busch, A. Waniuk, and W.L. Johnson J. Non-Cryst. Solids, in press

[33] M.L. William, R.F. Landel, and J.D. Ferry, J. Am. Chem. Soc., **77**, 3701 (1955)

[34] C. Weißmantel and C. Hamann, *Grundlagen der Festkörperphysik* (Springer-Verlag 1980)

[35] M. Fogiel, *Handbook of Mathematical, Scientific, Engineering Formulas, Tables, Functions, Graphs, Transformations* (Research & Education Association 1994)

[36] A. Masuhr and U. Geyer, unpublished

[37] A. Meyer, J. Wuttke, W. Petry, O.G. Randl, and H. Schober, Phys. Rev. Lett. **80**, 4454 (1998)

[38] T.E. Faber, *Introduction to the Theory of Liquid Metals* (Cambridge University Press, 1972)

[39] R. Busch and W.L. Johnson, Mat. Sci Forum **269-272**, 577 (1998)

[40] M.D. Ediger, C.A. Angell, and S.R. Nagel, J. Phys. Chem. **100**, 13200 (1996)

[41] W.N. Findley, J.S. Lai, and K. Onaran, *Creep and Relaxation of Nonlinear Viscoelastic Materials* (North-Holland, 1976)

[42] C.A. Angell, D.R. MacFarlane, and M. Oguni, Annals of the New York Academy of Science, **484**, 241 (1986)

[43] W.L. Johnson, Mat. Sci Forum **225-227**, 35 (1996)

[44] K. Knorr, private communications

[45] H. Ehmler, A. Heesemann, K. Rätzke, F. Faupel, and U. Geyer, Phys. Rev. Lett. **80**, 4919 (1998)

[46] K.F. Kelton, Solid State Physics, **45**, 75 (1991)

[47] D.M. Herlach, Mat. Sci. Eng. **R12**, 177 (1994)

[48] R. Busch, S. Schneider, A. Peker, and W.L. Johnson, Appl. Phys. Lett. **67**, 1544 (1995)

[49] S. Schneider, P. Thiyagarajan, and W.L. Johnson, Appl. Phys. Lett. **68**, 493 (1996)

[50] K.F. Kelton, Phil. Mag. Lett. **77**, 337 (1998)

[51] S. Schneider, P. Thiyagarajan, and W.L. Johnson, Appl. Phys. Lett. **68**, 493 (1996)

[52] K.F. Kelton, Phil. Mag. Lett. **77**, 337 (1998)

[53] D.R. Uhlmann, J. Non-Cryst. Solids **7**, 337 (1972)

[54] H.A. Davies, Physics and Chemistry of Glasses **17**, 159 (1976)

[55] Y.J. Kim, R. Busch, W.L. Johnson, A.J. Rulison, and W.K. Rhim, Appl. Phys. Lett. **68**, 1057 (1996)

[56] A. Wiedemann, U. Keiderling, M.P. Macht, and H. Wollenberger, Mat. Sci. Forum **225-227**, 71 (1996)

[57] Y.J. Kim, R. Busch, W.L. Johnson, A.J. Rulison, and W.K. Rhim, Appl. Phys. Lett. **65**, 2136 (1994)

[58] J. Schroers, R. Busch, A. Masuhr, and W.L. Johnson, Appl. Phys. Lett., in press

[59] A. Masuhr, R. Busch, and W.L. Johnson, Mater. Sci. Forum **269-272**, 779 (1998)

[60] F. Spaepen, Solid State Physics **42**, 1 (1994)

[61] U. Köster and Jürgen Meinhardt, Mater. Sci. Eng. **A178**, 271 (1994)

[62] R.W. Cahn, *Physical Metallurgy* (North-Holland 1983)

[63] W.L. Johnson, ASM Metals Handbook, **2**, 804 (1990)

[64] W. Wang, Q. Wei, and H.Y. Bai, Appl. Phys. Lett. **71**, 58 (1997)

[65] J. Schroers, private communications

[66] T. Hashimoto, K. Matsuzaka, E. Moses, and A. Onuki, Phys. Rev. Lett. **74**, 126 (1994)

[67] I. Gutzow, A. Dobreva, and J. Scmelzer, J. Mater. Sci. **28**, 890 (1993)

[68] L. Heyman, E. Noack, and L. Kaempfe, Mater. Sci. Eng. **A196**, 261 (1995)

[69] R.G. Larson, Rheol. Acta, **31**, 497 (1992)

[70] R. Horst and B.A. Wolf, Rheol. Acta, **33**, 99 (1994)

[71] P. Padilla and S. Toxvaerd, J. Chem. Phys., **106**, 2342 (1996)